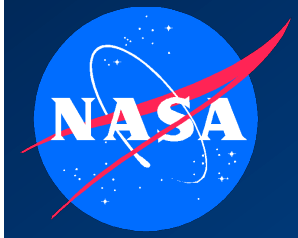

Measuring and Modeling the Transport of Magnetic Flux at the Surface of the Sun:

Toward Solving one-half of the Solar Dynamo Problem

Dr. David H. Hathaway
NASA/ARC-TN

2014 August 26
AMS Seminar

Outline

- The Sunspot Cycle
- The Sun's Magnetic Dynamo
- Surface Flux Transport
- Measuring the Flows
- Modeling the Transport
- Space Weather Predictions

The Sunspot Cycle

Sunspot Cycle Discovery

Astronomers had been observing sunspots for over 230 years before Heinrich Schwabe, an amateur astronomer in Dessau, Germany, discovered in 1844 that the number of sunspot groups and the number of days without sunspots increased and decreased in cycles of about 10-years.

Schwabe's data for 1826 to 1843

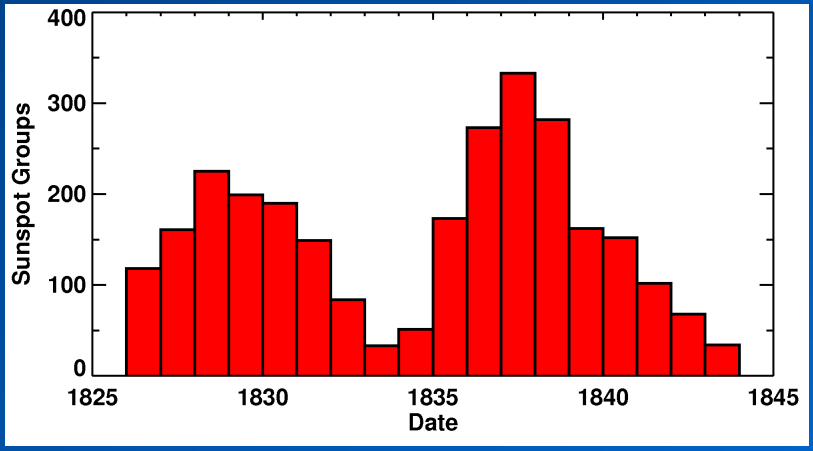

Number of Sunspot Groups per Year

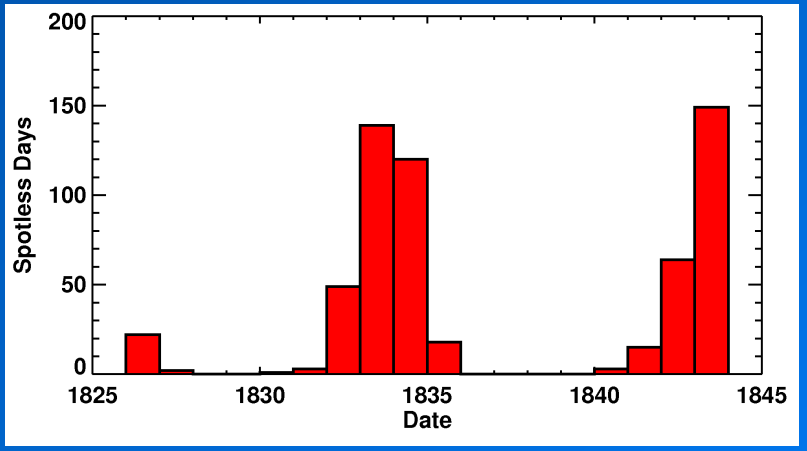

Number of Spotless Days

23 Full Cycles

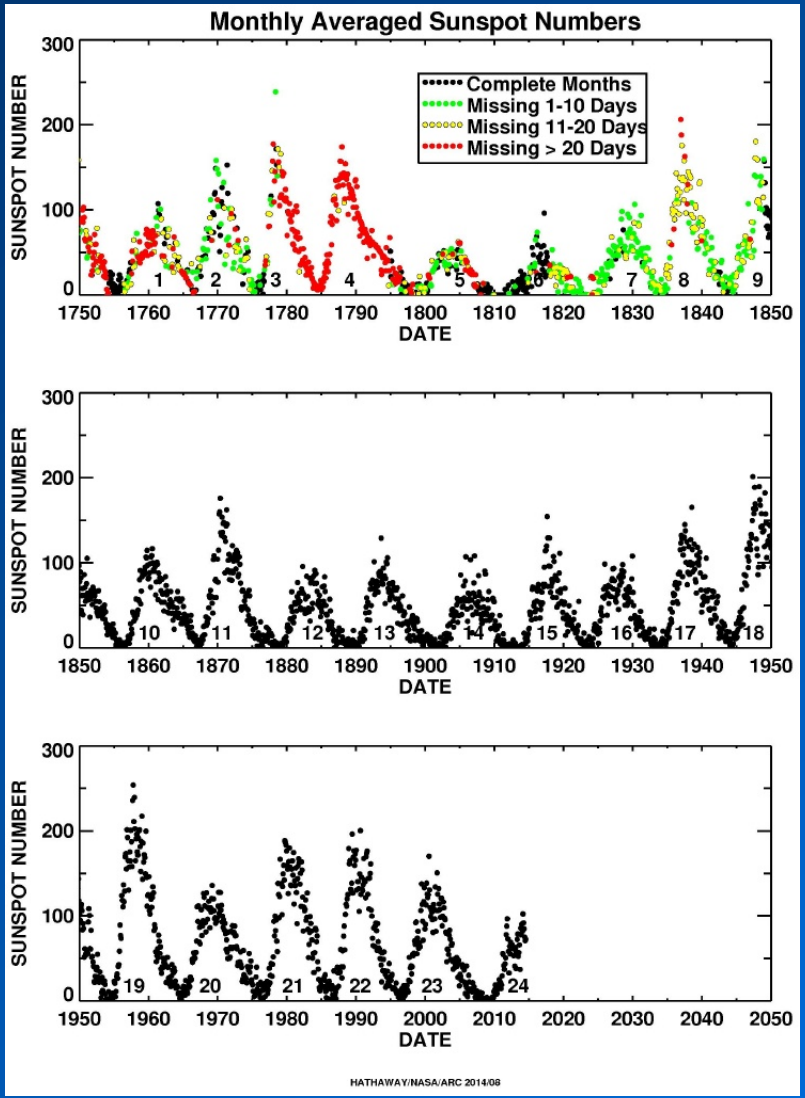

Shortly after Schawbe's discovery Rudolf Wolf proposed using a "Relative" Sunspot Number count. While there were many days without observations prior to 1849, sunspots have been counted on every day since. To this day we continue to use Wolf's Relative Sunspot Number and his cycle numbering.

The average cycle lasts about 11 years, but with a range from 9 to 14.

The average amplitude is about 100, but with a range from 50 to 200.

Sunspot Latitudes

Sunspots appear in two bands on either side of the equator. These bands drift toward the equator as the cycle progresses. Big cycles have wider bands that extend to higher latitudes. Cycles typically overlap by 2-3 years.

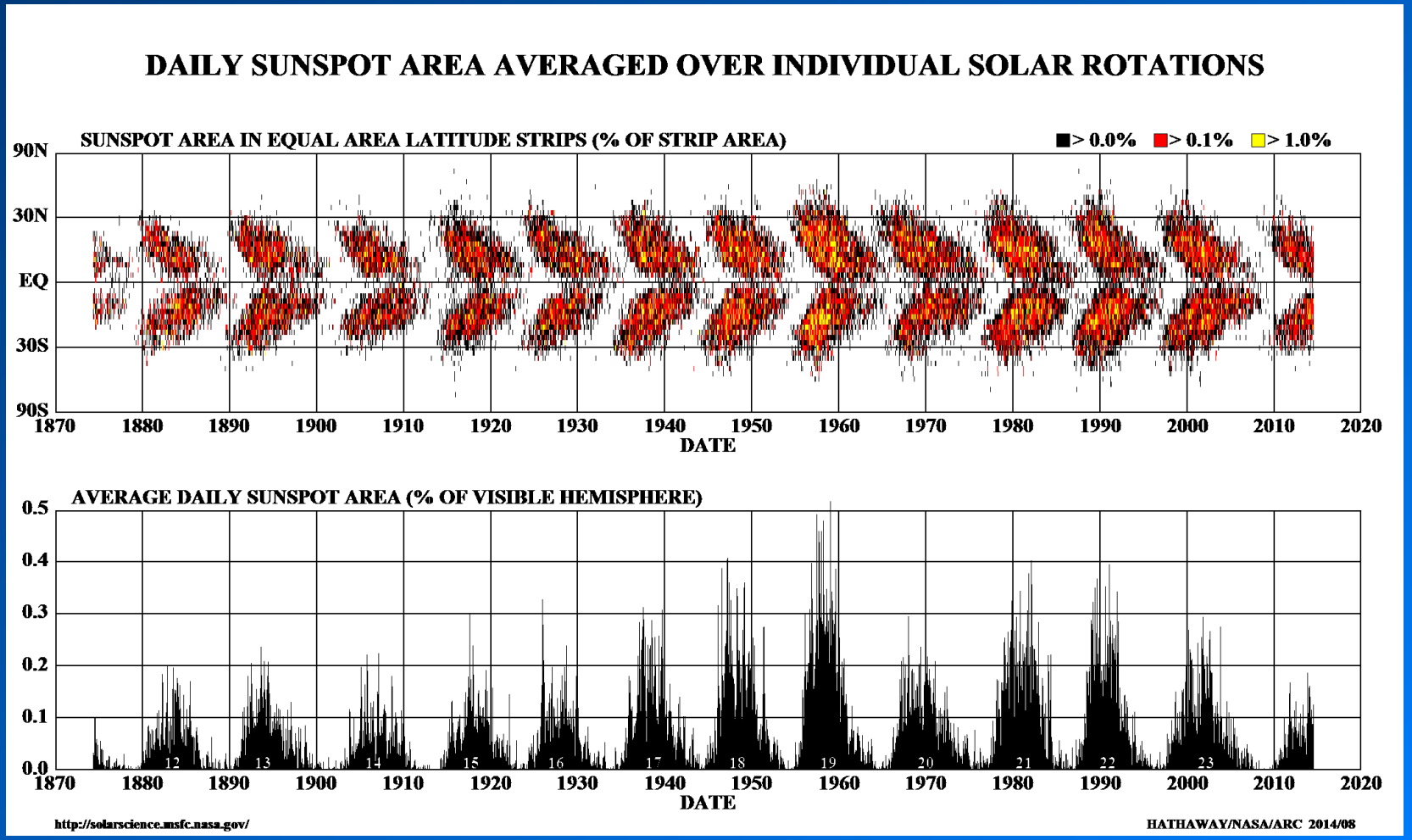

Sunspot Group Tilt- Joy's Law

Sunspot groups are tilted with the leading spots (the spots seen first as the Sun rotates) closer to the equator than the following spots. In 1919 Alfred Joy noted that this tilt increases with latitude on the Sun.

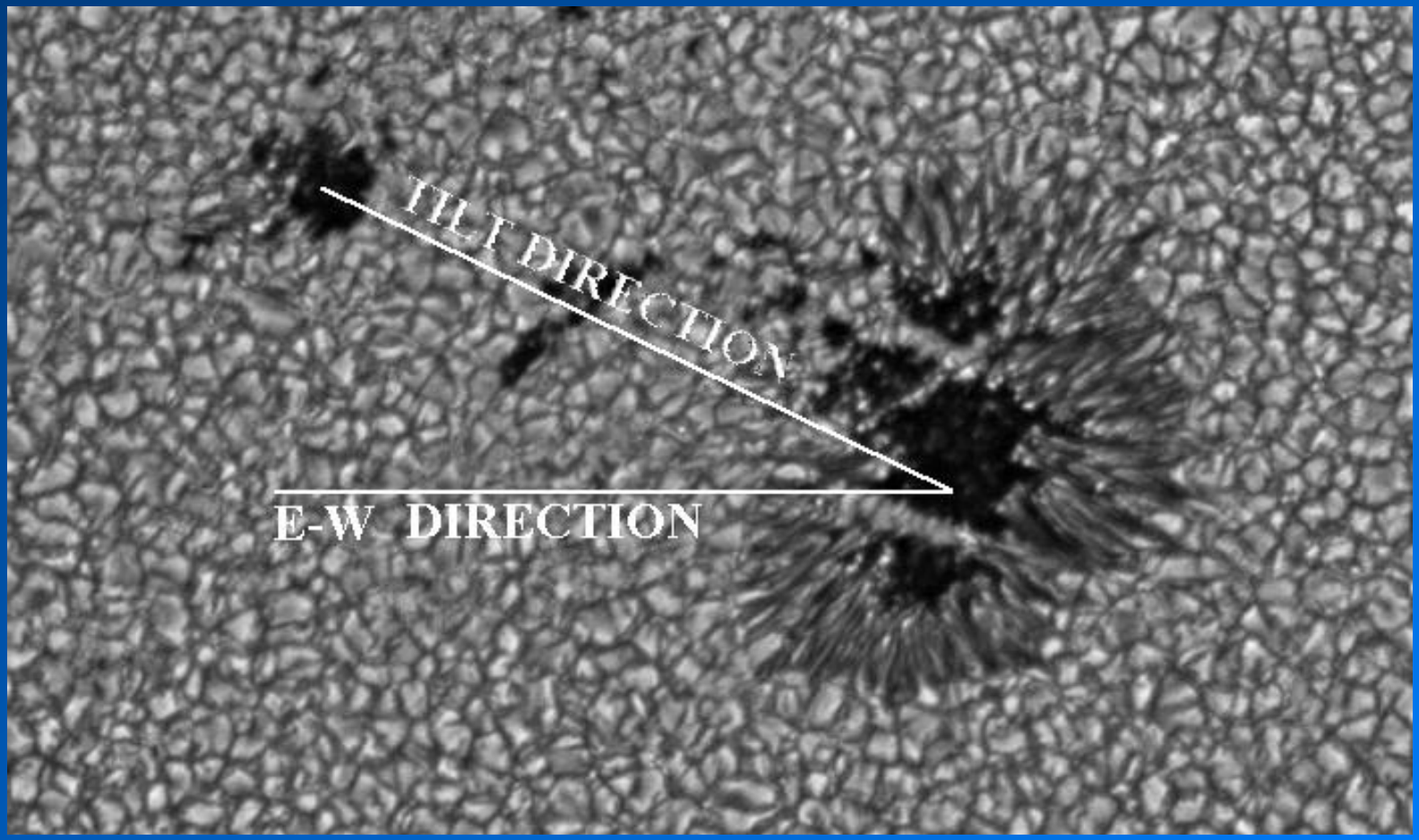

Solar Magnetism – The Key

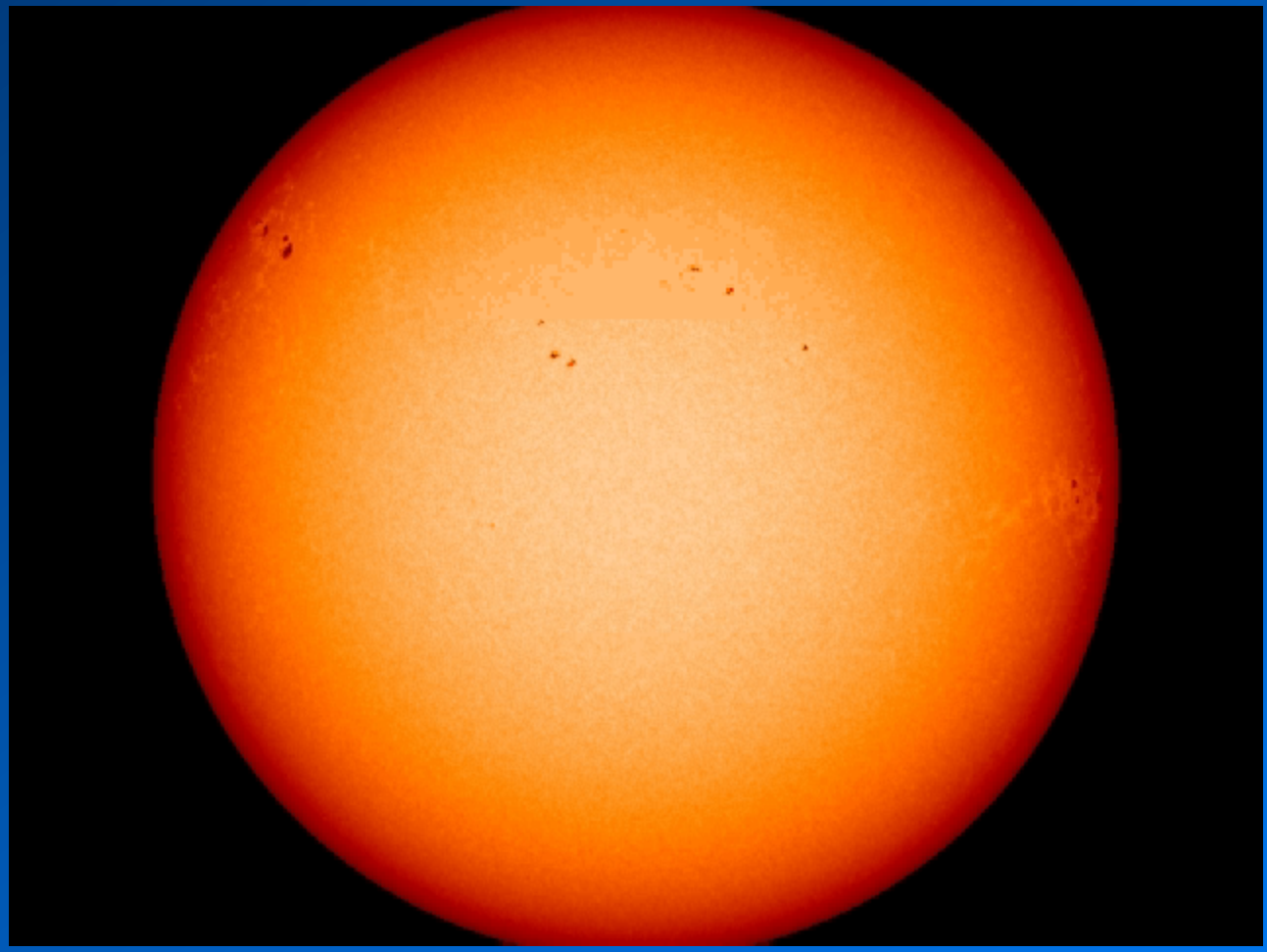

Hale's Magnetic Polarity Law

In 1919 George Ellery Hale found that the magnetic field in sunspots followed a definite law, "Hale's Law" such that: *"...the preceding and following spots ... are of opposite polarity, and that the corresponding spots of such groups in the Northern and Southern hemispheres are also opposite in sign. Furthermore, the spots of the present cycle are opposite in polarity to those of the last cycle".*

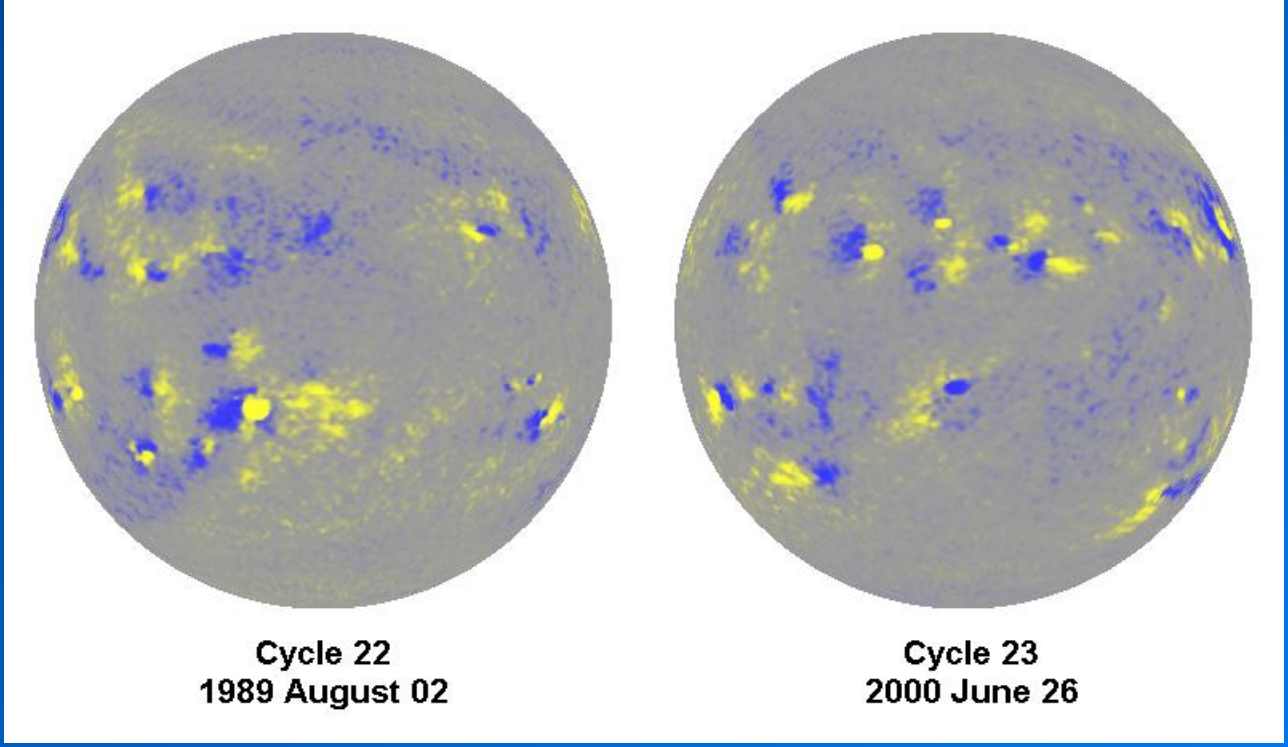

Cycle 22
1989 August 02

Cycle 23
2000 June 26

Three Solar Cycles in Action

In addition to these magnetic polarity changes and the equatorward drift of the sunspot latitudes, there are important flows on the surface and within the Sun: ***Differential Rotation*** – faster at the equator, slower near the poles; and ***Meridional Flow*** – flow from the equator toward the poles along the surface.

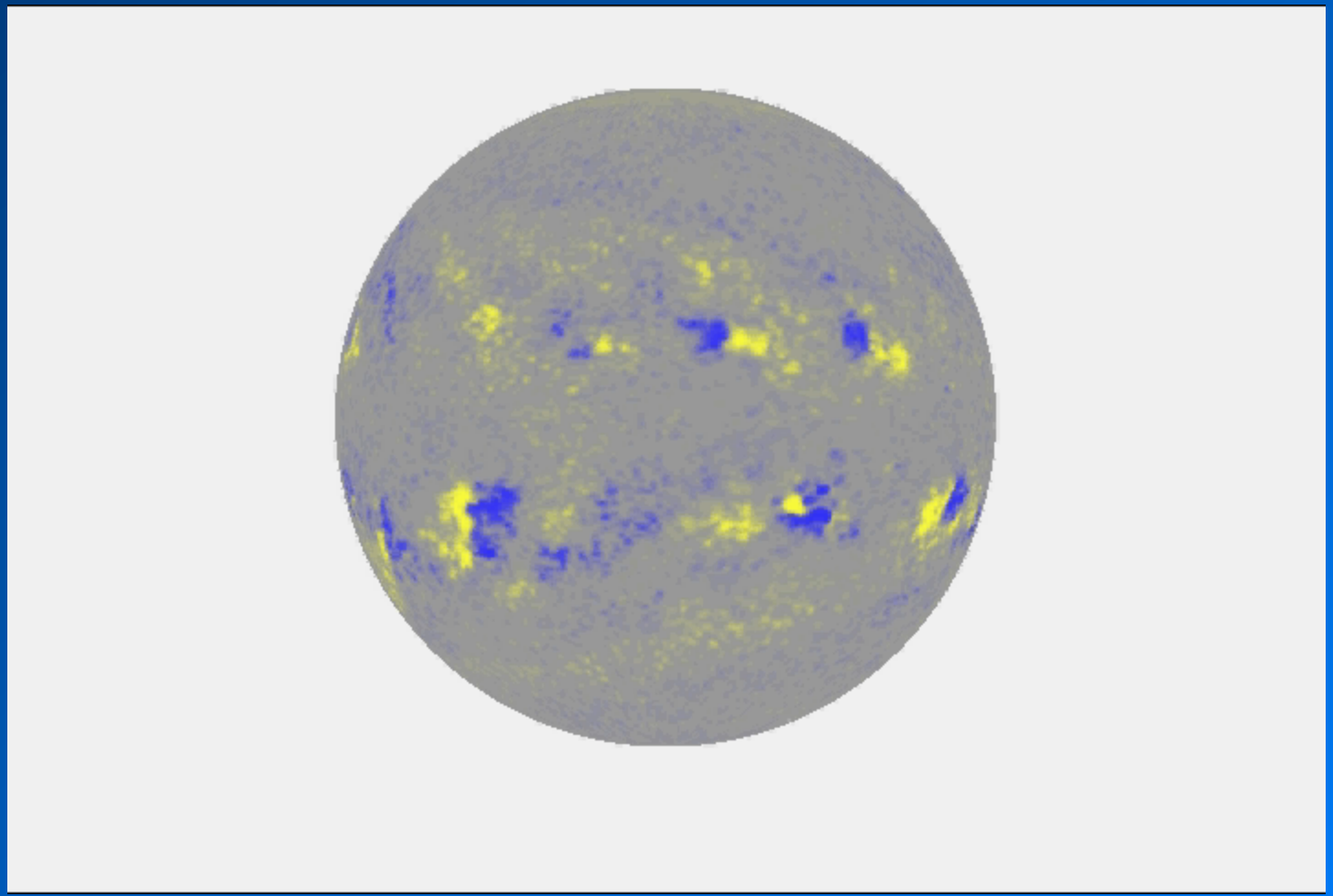

Polar Field Reversals

In 1958 Horace Babcock and Bill Livingston noted that the magnetic polarities of the Sun's weak polar fields also reverse from one cycle to the next, and that this reversal happens at about the time of sunspot cycle maximum (the South reversed in 1957 the North in 1958).

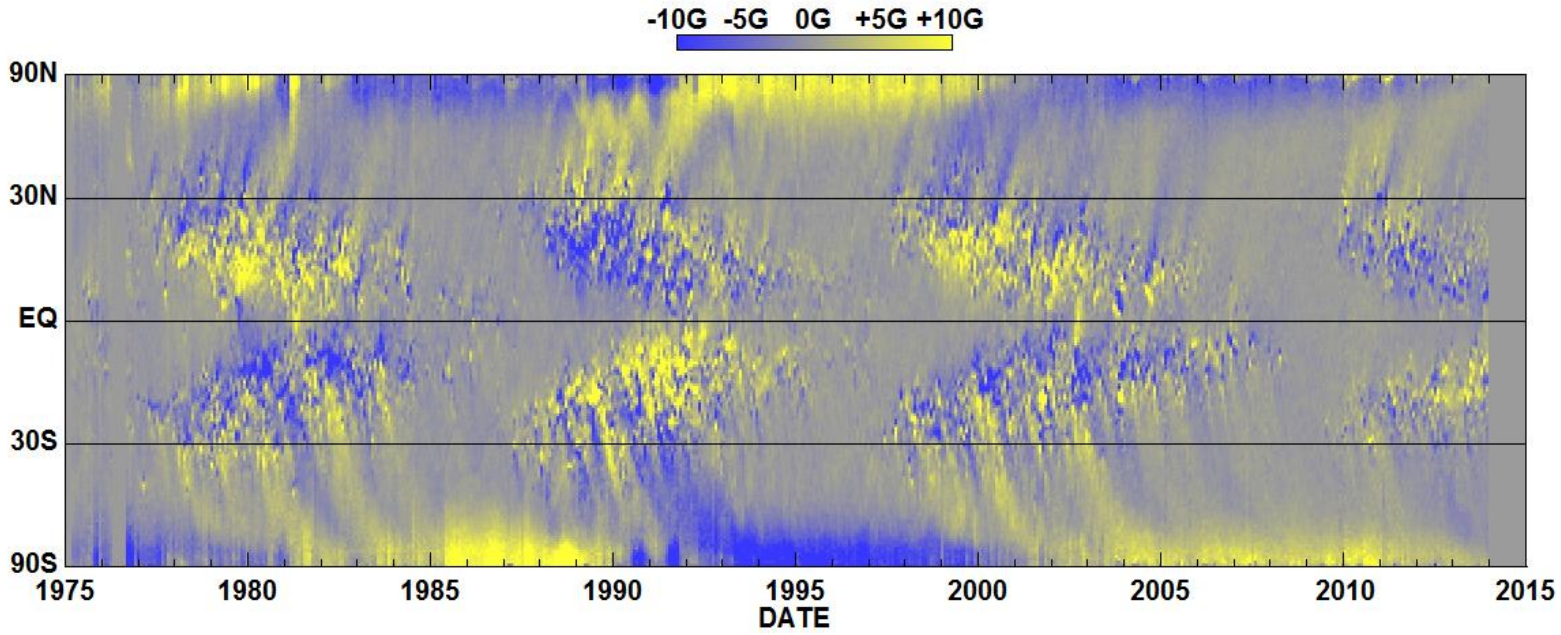

The Sun's Magnetic Dynamo

Babcock's Dynamo (1961)

Dynamo models have been developed to explain the sunspot cycle.

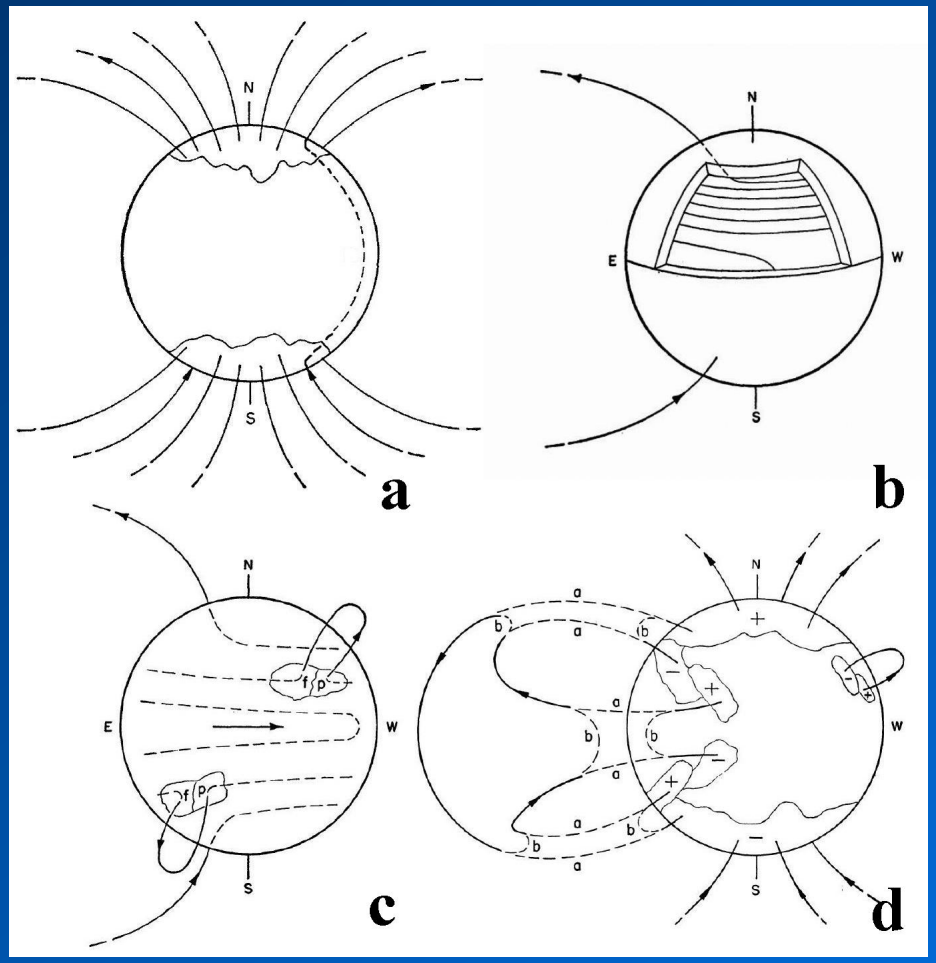

a) Dipolar field at cycle minimum threads through a shallow layer below the surface.

b) Differential rotation shears out this poloidal field to produce a strong toroidal field (first at the mid-latitudes then progressively lower latitudes).

c) Buoyant fields erupt through the photosphere giving Hale's polarity law and Joy's Law.

d) Meridional transport cancels preceding polarities across the equator and carries following polarity to the poles.

Polar Fields – Seeds for Cycles

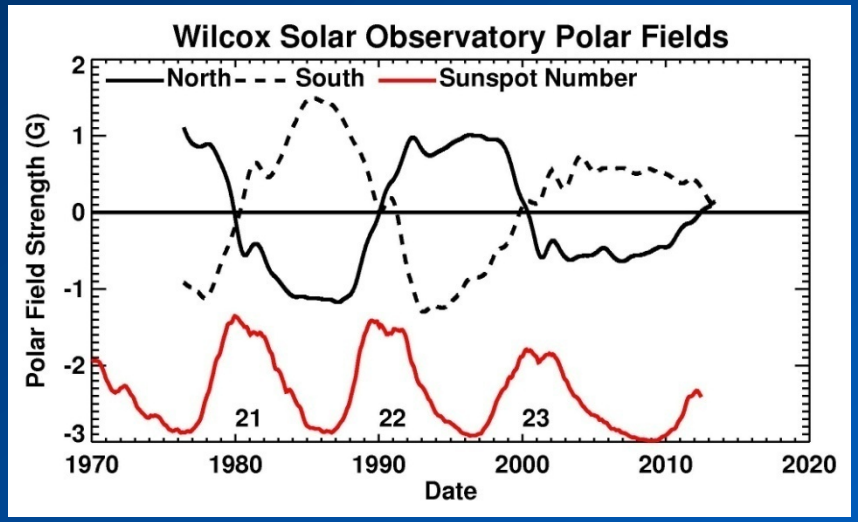

The Sun's polar fields are the seeds of the next solar cycle in these dynamo models. We have direct observations for the last three cycles and a proxy (polar faculae) for the last 10 cycles.

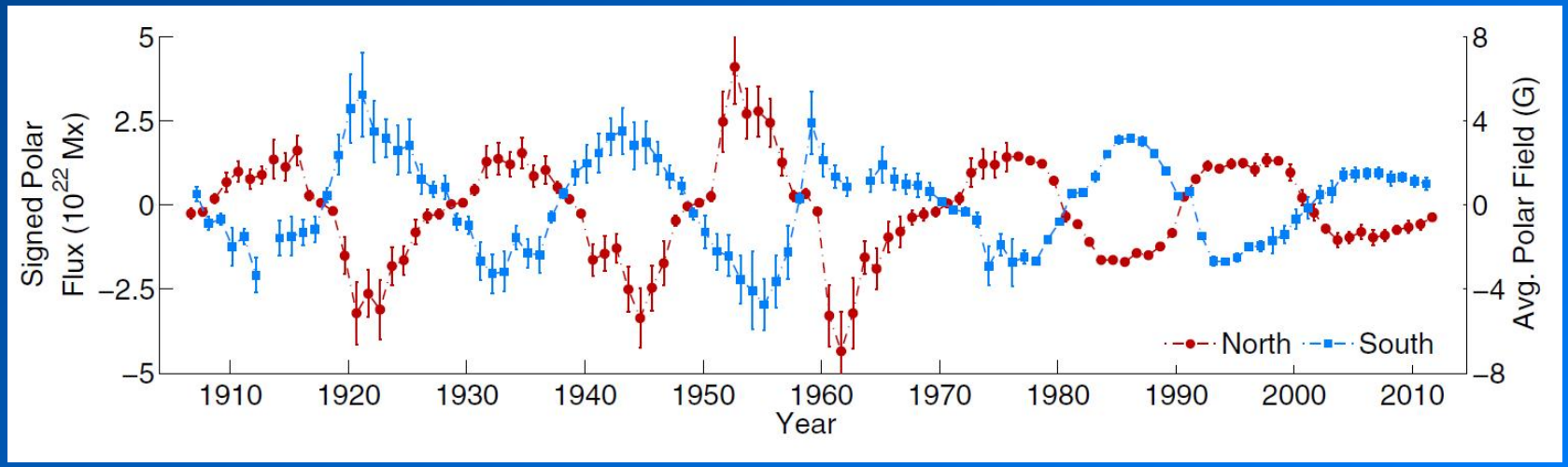

Polar Fields as Predictors

There is a strong correlation between polar fields and the amplitude of the next solar cycle (hemisphere by hemisphere in terms of peak sunspot area).

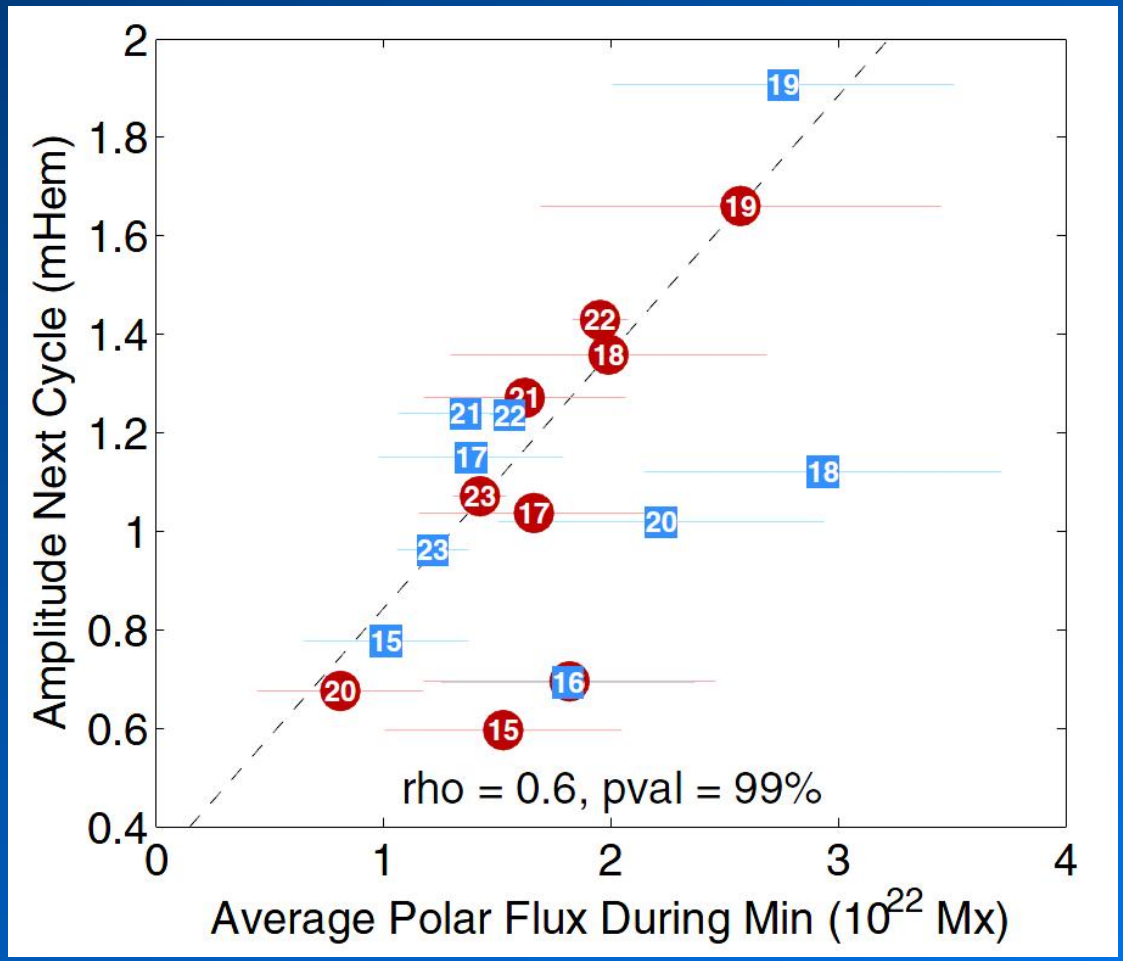

North – Blue squares
South – Red circles

Cycles 21-23 are from direct magnetic measurements.

Earlier cycles are from counting polar faculae.

How are Polar Fields Made?

Back to Babcock (1961)

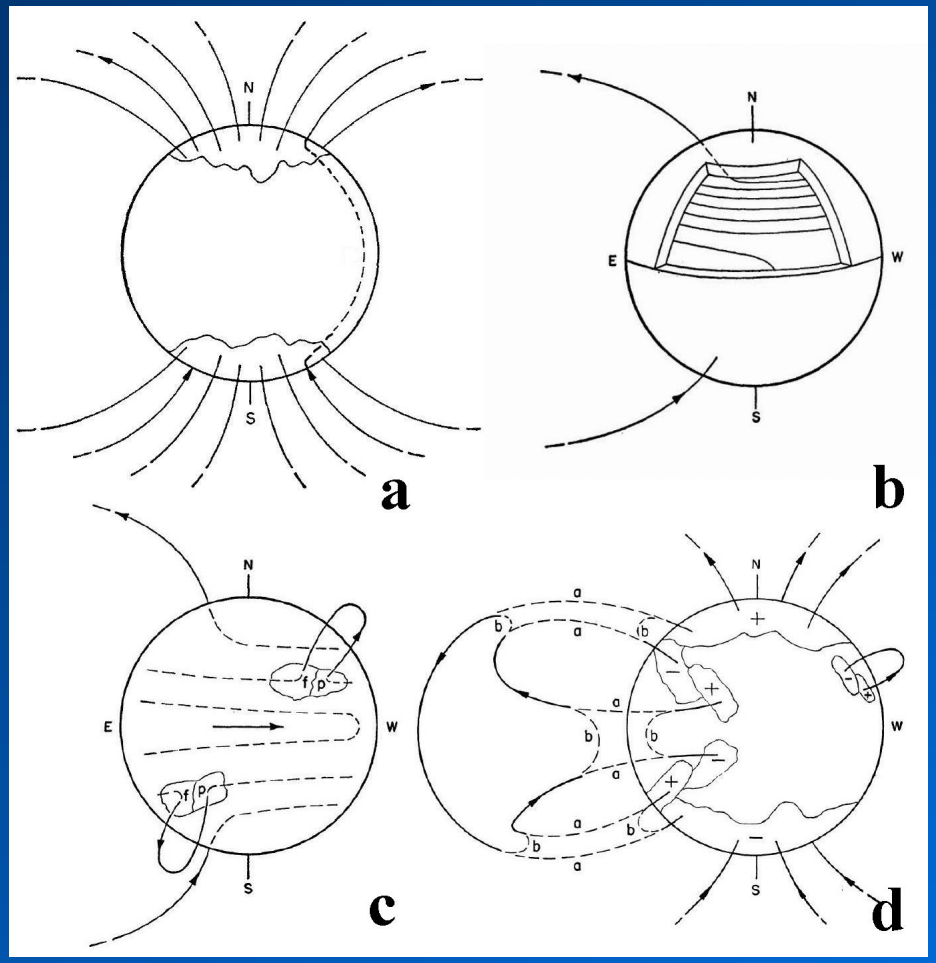

a) Dipolar field at cycle minimum threads through a shallow layer below the surface.

b) Differential rotation shears out this poloidal field to produce a strong toroidal field (first at the mid-latitudes then progressively lower latitudes).

c) Buoyant fields erupt through the photosphere giving Hale's polarity law and Joy's Law.

d) Meridional transport cancels preceding polarities across the equator and carries following polarity to the poles.

What Makes the Polar Fields?

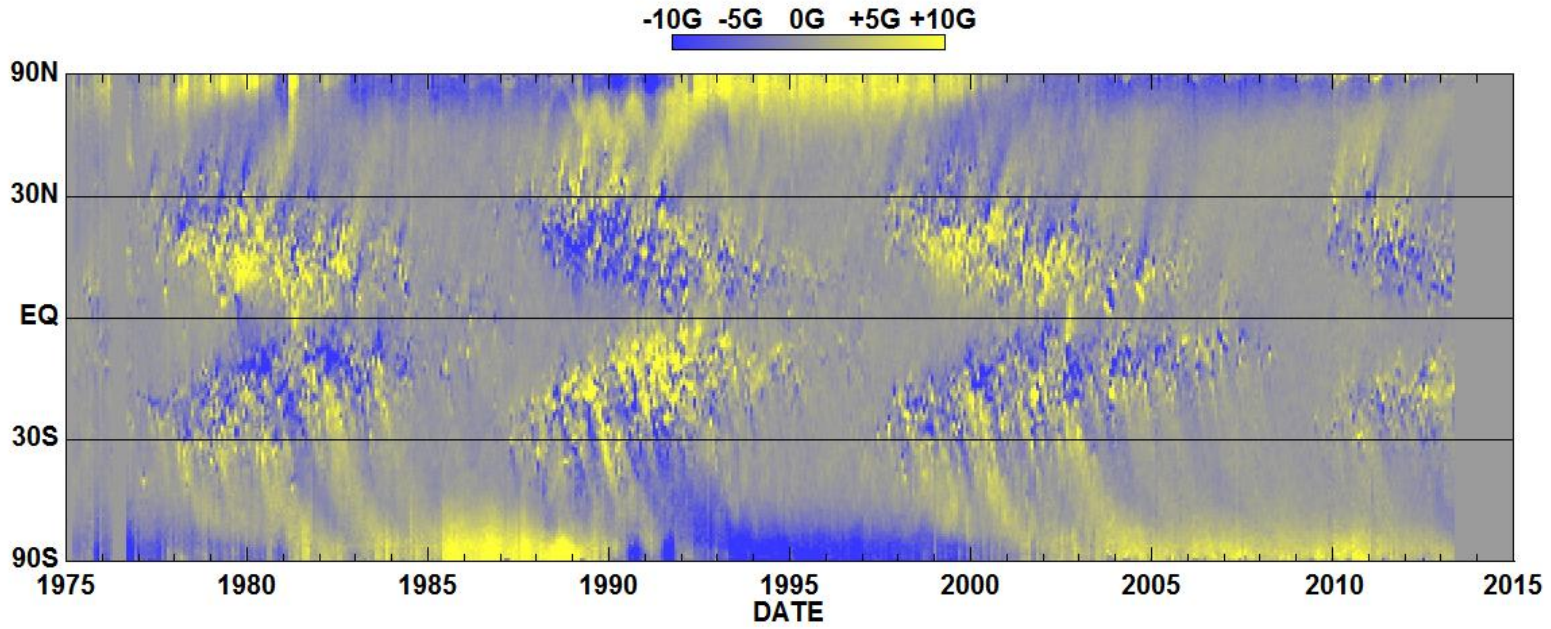

Tilted active regions and flux transport.

Surface Flux Transport

Surface Flux Transport

Surface magnetic flux transport models were developed in the early 1980s by the Naval Research Laboratory (NRL) group including Neil Sheeley, Yi-Ming Wang, Rick DeVore, and Jay Boris. They found that they could reproduce the evolution of the Sun's surface magnetic field using active region flux emergence as the only source of magnetic flux – that flux is then transported across the Sun's surface by:

1. Differential Rotation, $V_\phi(\theta)$
2. Meridional Flow, $V_\theta(\theta)$
3. Supergranule Diffusion, κ

$$\partial B/\partial t + 1/(R \sin\theta)\, \partial(BV \sin\theta)/\partial\theta + 1/(R \sin\theta)\, \partial(BU)/\partial\phi = \kappa \nabla^2 B + S(\theta,\phi)$$

Neither the meridional flow nor the supergranule diffusion were well constrained at that time – so they used what worked.

Supergranule Diffusion

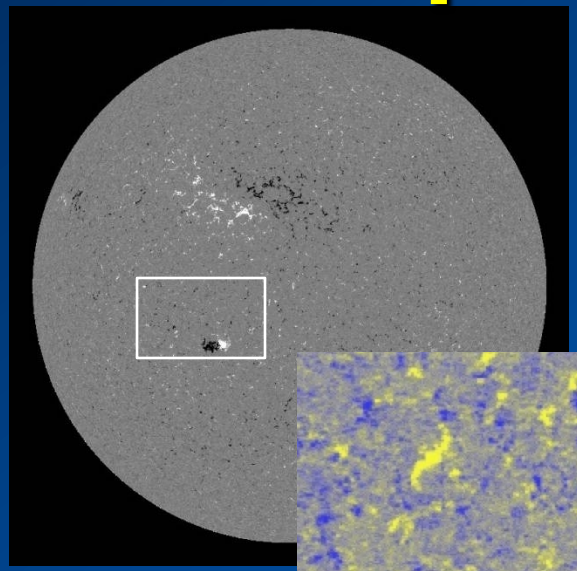

Four days of HMI data drive home the fact that flux transport is dominated by the cellular flows. The extent to which this can be represented by a diffusion coefficient and a Laplacian operator is to be determined.

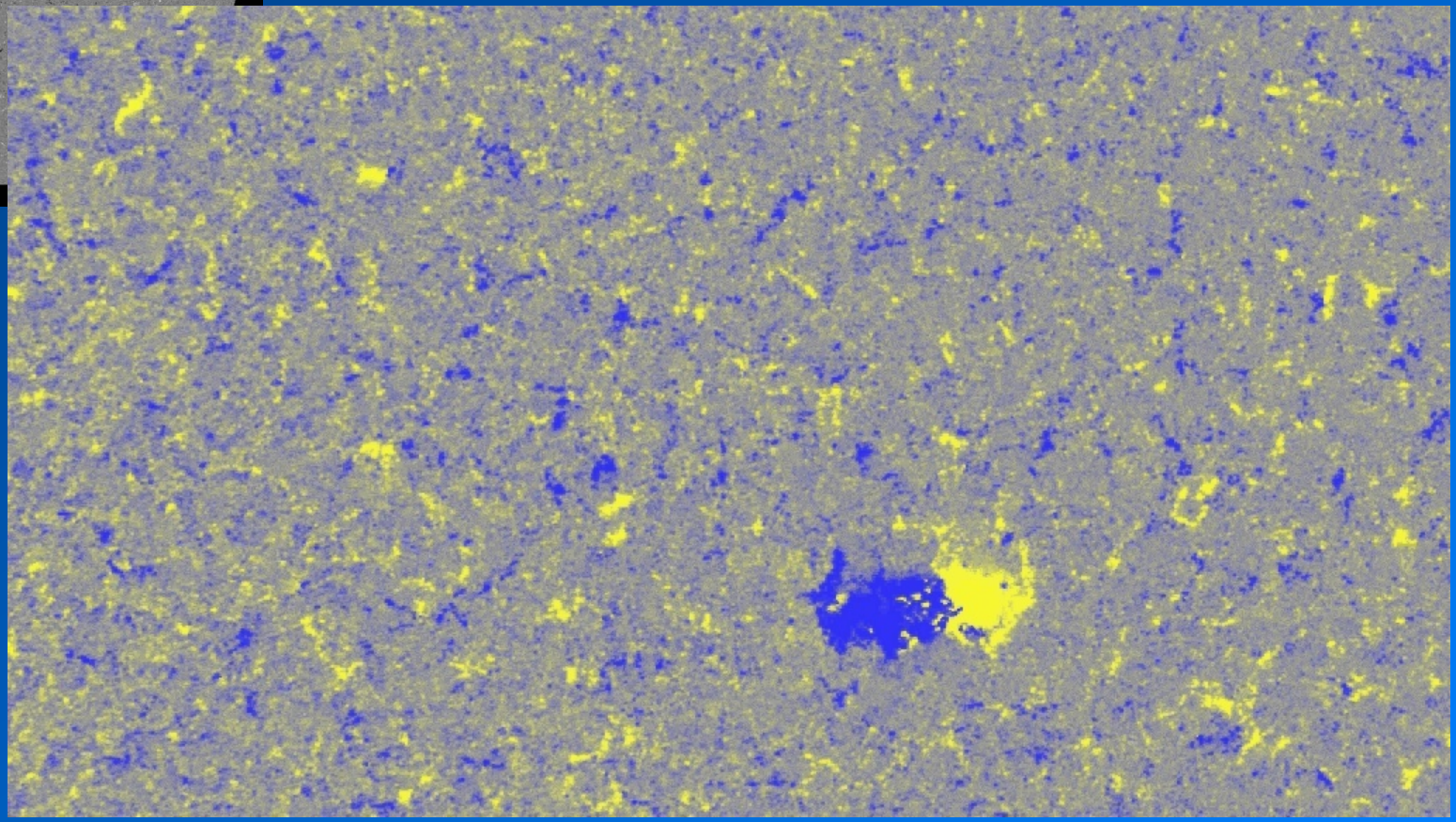

Supergranules and the Magnetic Network

Tracking the motions of granules (Local Correlation Tracking with 6-minute time lags from HMI Intensity data) reveals the flow pattern within supergranules and the relationship to the magnetic pattern – the magnetic network forms at the supergranule boundaries (convergence zones).

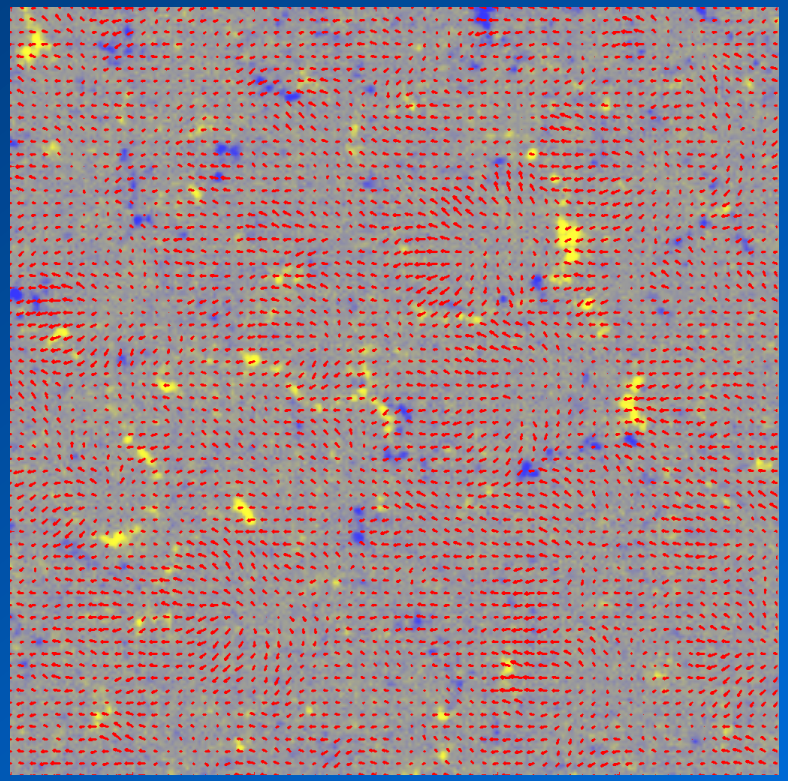

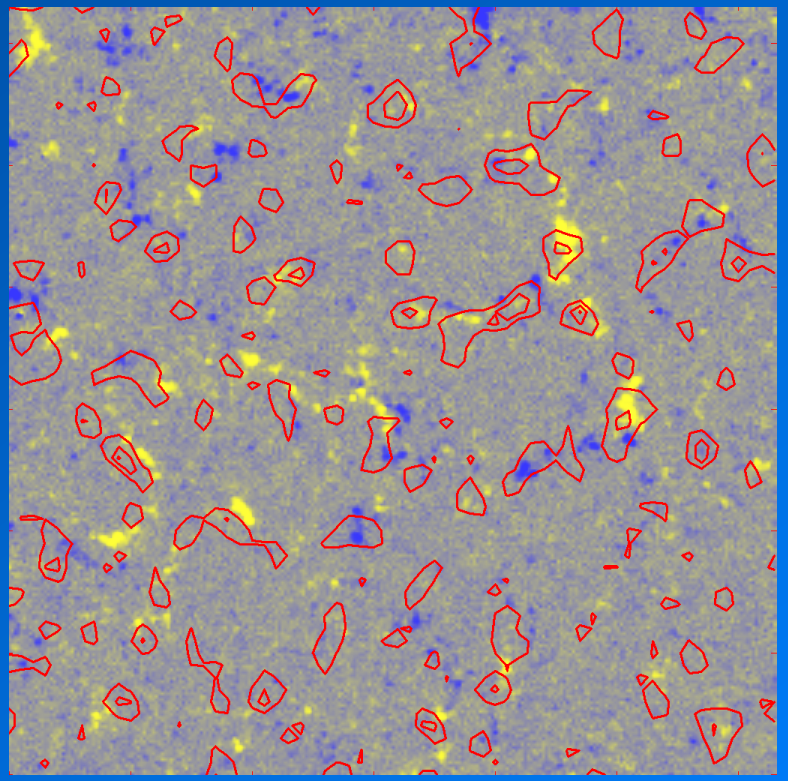

Goals

- Produce a surface flux transport model based on observations
  - Characterize the axisymmetric flows
  - Characterize the non-axisymmetric flows
  - Produce “synchronic” maps of the entire surface for comparison with observations
- Determine any missing processes
  - Are active regions the only sources?
  - Is 2D sufficient or are there 3D processes?
- Use these synchronic maps for space weather applications
  - Coronal and Interplanetary field configuration

Measuring the Flows

Characterizing and Modeling Supergranules

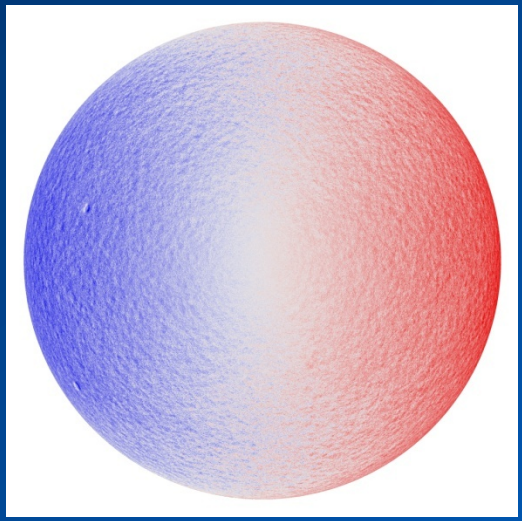

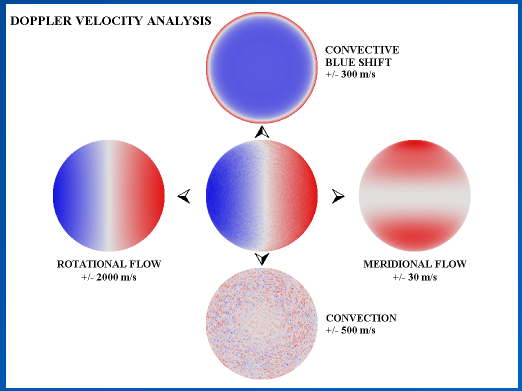

The line-of-sight Doppler velocity signal due to supergranules was first noted by Avril Hart (1954) but Leighton, Noyes, and Simon (1962) were the first to image them and call them supergranules.

In a series of papers starting in 1988 I have developed an analysis and modeling method based on vector spherical harmonics.

The first step is to determine and remove the Doppler signals due to the axisymmetric flows (differential rotation and meridional flow) and due to the unresolved granules (convective blue shift).

Simulated Data

$$V_r(\theta,\phi) = \sum_{l=0}^{l\max} \sum_{m=-l}^{l} R_l^m Y_l^m(\theta,\phi)$$

$$V_\theta(\theta,\phi) = \sum_{l=1}^{l\max} \sum_{m=-l}^{l} S_l^m \frac{\partial Y_l^m(\theta,\phi)}{\partial\theta} + \sum_{l=1}^{lmax} \sum_{m=-l}^{l} T_l^m \frac{1}{\sin\theta} \frac{\partial Y_l^m(\theta,\phi)}{\partial\phi}$$

$$V_\phi(\theta,\phi) = \sum_{l=1}^{l\max} \sum_{m=-l}^{l} S_l^m \frac{1}{\sin\theta} \frac{\partial Y_l^m(\theta,\phi)}{\partial\phi} - \sum_{l=1}^{l\max} \sum_{m=-l}^{l} T_l^m \frac{\partial Y_l^m(\theta,\phi)}{\partial\theta},$$

Vector velocities are constructed from a spectrum of radial (R), solenoidal (S), and toroidal (T) coefficients.

These velocities are then used to produce an image of the line-of-sight Doppler velocities.

Both the observed velocity image and the simulated velocity image are projected onto spherical harmonics and the resulting kinetic energy spectra are compared.

$$V_{\text{los}}(\theta,\phi) = V_r(\theta,\phi)\sin B_0\cos\theta + V_r(\theta,\phi)\cos B_0\sin\theta\cos\phi + V_\theta(\theta,\phi)\sin B_0\sin\theta - V_\theta(\theta,\phi)\cos B_0\cos\theta\cos\phi + V_\phi(\theta,\phi)\cos B_0\sin\phi,$$

Supergranule Spectrum

In a series of papers we (Hathaway et al. 2000, 2002, 2010) analyzed and simulated Doppler velocity data from MDI to determine the characteristics of supergranulation. These cellular flows have a broad spectrum characterized by a peak in power at wavelengths of ~35 Mm.

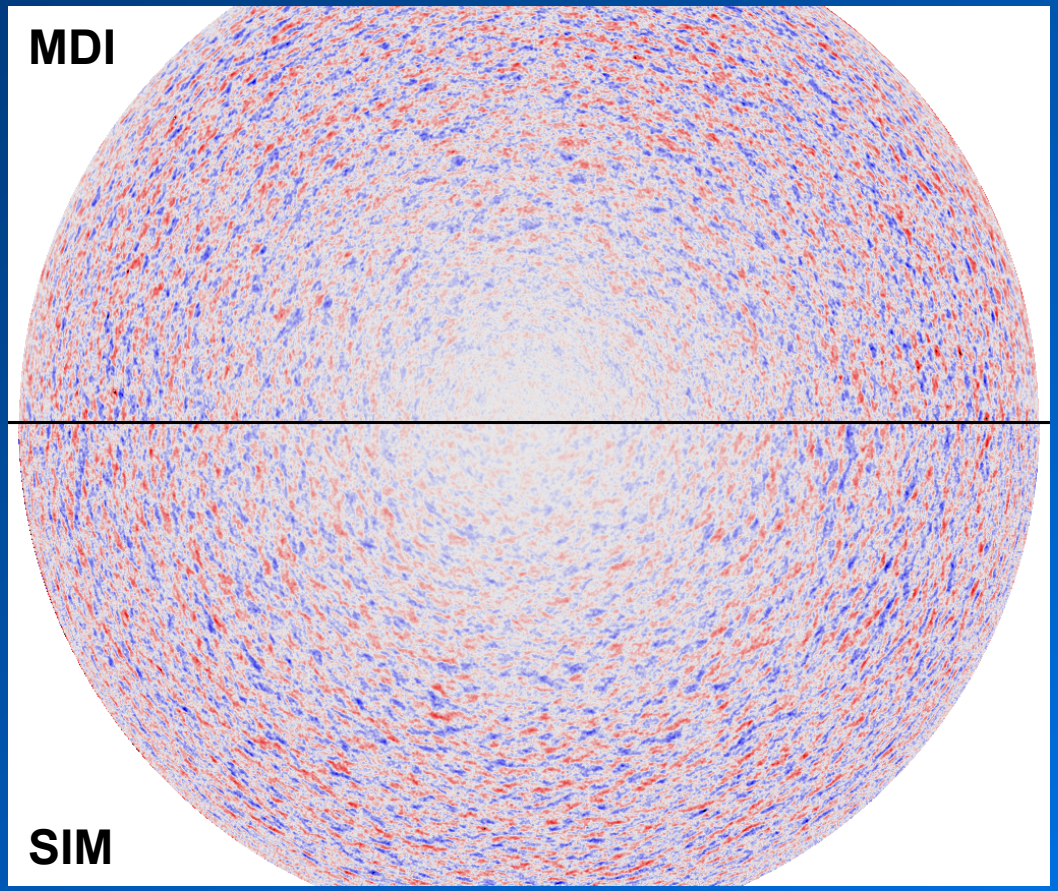

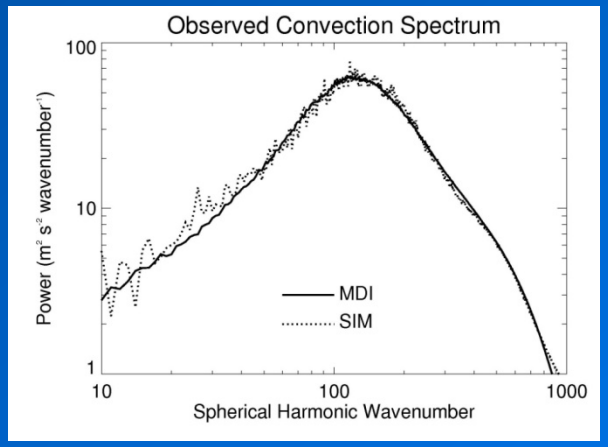

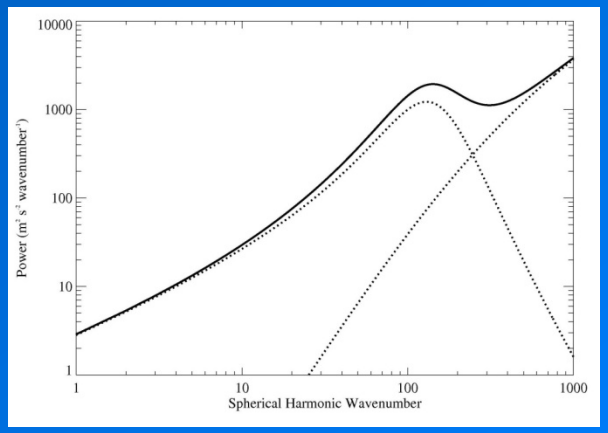

Supergranule Time Evolution

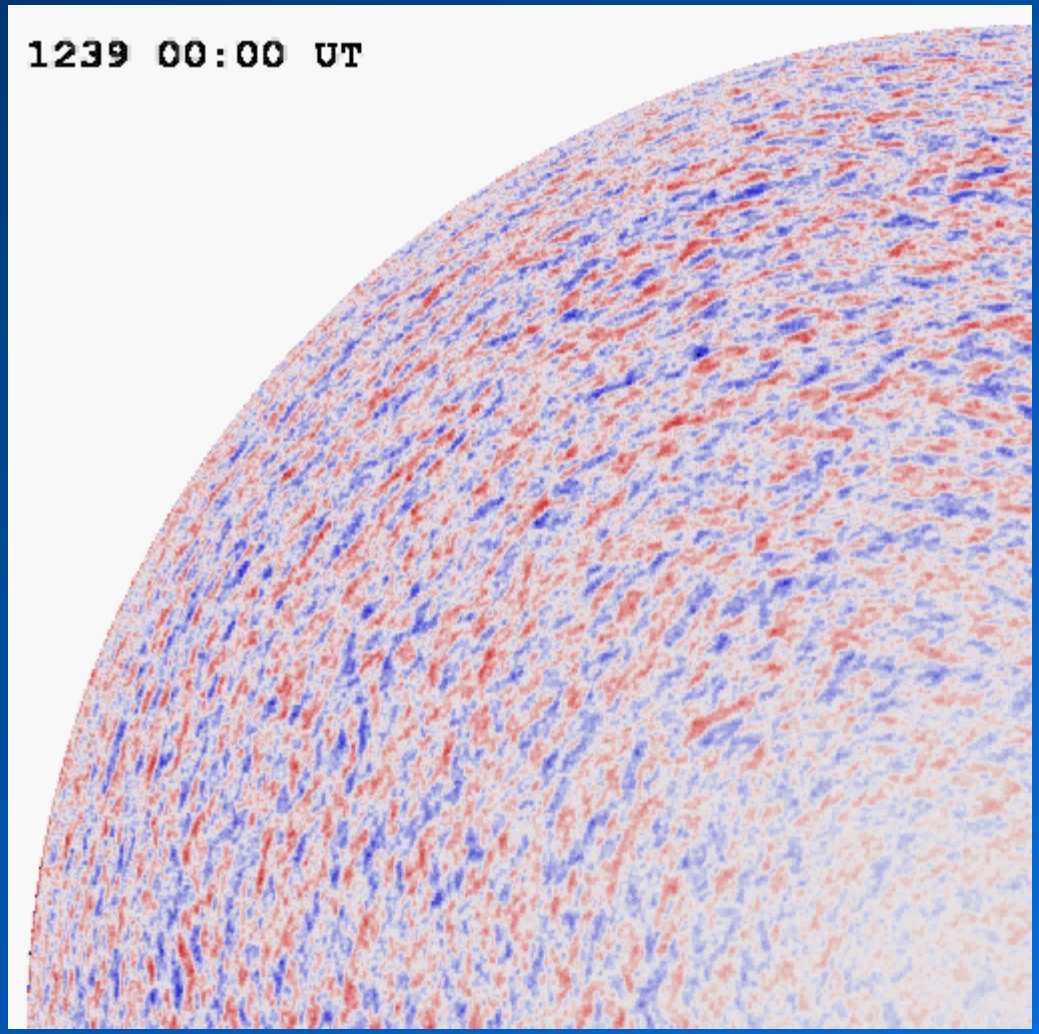

The supergranule pattern rotates with the Sun's rotation and evolves on a time scale of hours to days depending on cell size.

Modeling this requires calculating the time evolution of the spectral coefficients.

Spectral Coefficient Evolution

$$\frac{\partial R_\ell^m}{\partial t} = -\frac{V_0}{r}\left[\frac{(\ell-2)}{A_\ell^m A_{\ell-1}^m} R_{\ell-2}^m + \left[\frac{\ell B_{\ell+2}^m}{A_{\ell+2}^m A_{\ell+1}^m} - \frac{(\ell+1)}{A_\ell^m A_\ell^m}\right] R_\ell^m \right.$$
$$\left. - \frac{(\ell+3)B_{\ell+2}^m}{A_{\ell+2}^m A_{\ell+2}^m} R_{\ell+2}^m\right] - im\Omega_0 R_\ell^m - im\Omega_2\left[\frac{1}{A_\ell^m A_{\ell-1}^m} R_{\ell-2}^m \right.$$
$$\left. + \left[\frac{B_{\ell+2}^m}{A_{\ell+2}^m A_{\ell+1}^m} + \frac{B_{\ell+1}^m}{A_{\ell+1}^m A_\ell^m}\right] R_\ell^m + \frac{B_{\ell+3}^m}{A_{\ell+3}^m A_{\ell+2}^m} B_{\ell+2}^m R_{\ell+2}^m\right]$$
$$- im\Omega_4\left[\frac{1}{A_\ell^m A_{\ell-1}^m}\frac{1}{A_{\ell-2}^m A_{\ell-3}^m}\right] R_{\ell-4}^m - im\Omega_4$$
$$\times\left[\frac{B_{\ell+2}^m}{A_{\ell+2}^m A_{\ell+1}^m} + \frac{B_{\ell+1}^m}{A_{\ell+1}^m A_\ell^m} + \frac{B_\ell^m}{A_\ell^m A_{\ell-1}^m} + \frac{B_{\ell-1}^m}{A_{\ell-1}^m A_{\ell-2}^m}\right]\frac{1}{A_\ell^m A_{\ell-1}^m}$$
$$\times R_{\ell-2}^m - im\Omega_4\left[\frac{B_{\ell+3}^m}{A_{\ell+3}^m A_{\ell+2}^m} + \frac{B_{\ell+2}^m}{A_{\ell+2}^m A_{\ell+1}^m} + \frac{B_{\ell+1}^m}{A_{\ell+1}^m A_\ell^m}\right]$$
$$\times\frac{B_{\ell+2}^m}{A_{\ell+2}^m A_{\ell+1}^m} R_\ell^m - im\Omega_4\left[\frac{B_{\ell+2}^m}{A_{\ell+2}^m A_{\ell+1}^m} + \frac{B_{\ell+1}^m}{A_{\ell+1}^m A_\ell^m} + \frac{B_\ell^m}{A_\ell^m A_{\ell-1}^m}\right]$$
$$\times\frac{B_{\ell+1}^m}{A_{\ell+1}^m A_\ell^m} R_\ell^m - im\Omega_4\left[\frac{B_{\ell+4}^m}{A_{\ell+4}^m A_{\ell+3}^m} + \frac{B_{\ell+3}^m}{A_{\ell+3}^m A_{\ell+2}^m}\right.$$
$$\left. + \frac{B_{\ell+2}^m}{A_{\ell+2}^m A_{\ell+1}^m} + \frac{B_{\ell+1}^m}{A_{\ell+1}^m A_\ell^m}\right]\frac{B_{\ell+3}^m}{A_{\ell+3}^m A_{\ell+2}^m} B_{\ell+2}^m R_{\ell+2}^m$$
$$- im\Omega_4\left[\frac{B_{\ell+5}^m}{A_{\ell+5}^m A_{\ell+4}^m}\frac{B_{\ell+3}^m}{A_{\ell+3}^m A_{\ell+2}^m} B_{\ell+4}^m B_{\ell+2}^m\right] R_{\ell+4}^m. \qquad \text{(A12)}$$

The spectral coefficients are evolved in time to account for the advection of the pattern by the axisymmetric flows using the advection equation projected onto spherical harmonics.

This couples the evolution of one component to others with the same azimuthal order but different angular degree.

This is solved numerically using 4th order Runge-Kutta.

With ℓmax = 1500 the solutions are stable and well behaved using 15-minute time steps.

Measuring their motions

The axisymmetric flows can be measured using the Doppler velocity pattern and cross-correlation longitudinal strips from data obtained a few hours apart.

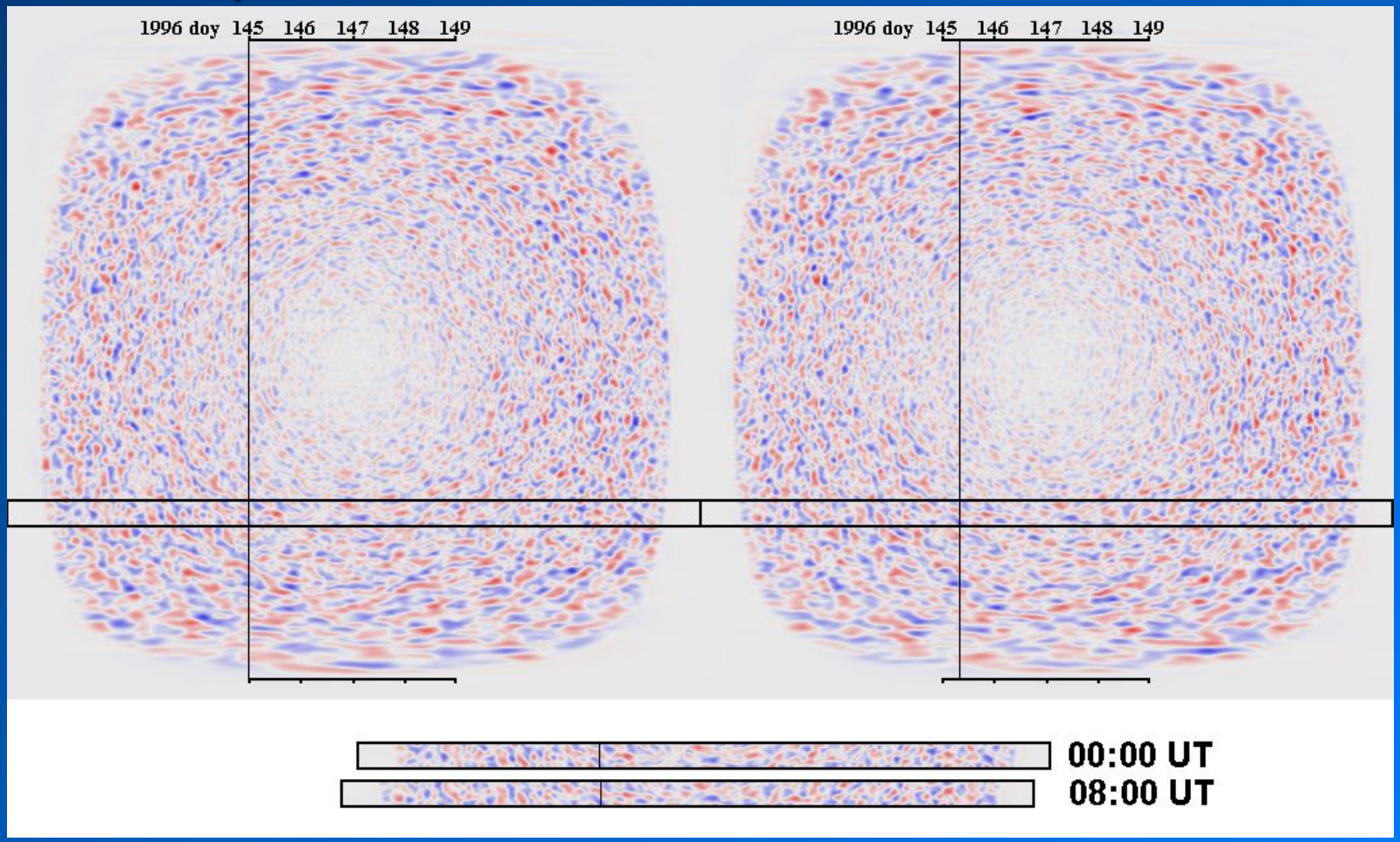

Reproducing their Rotation

The longitudinal motions of the cellular patterns can be reproduced by making systematic changes to the complex spectral coefficient phases (Hathaway et al. 2010). Black lines are polynomial fits to the observed signal. The colored dots in each diagram are measured from the simulation.

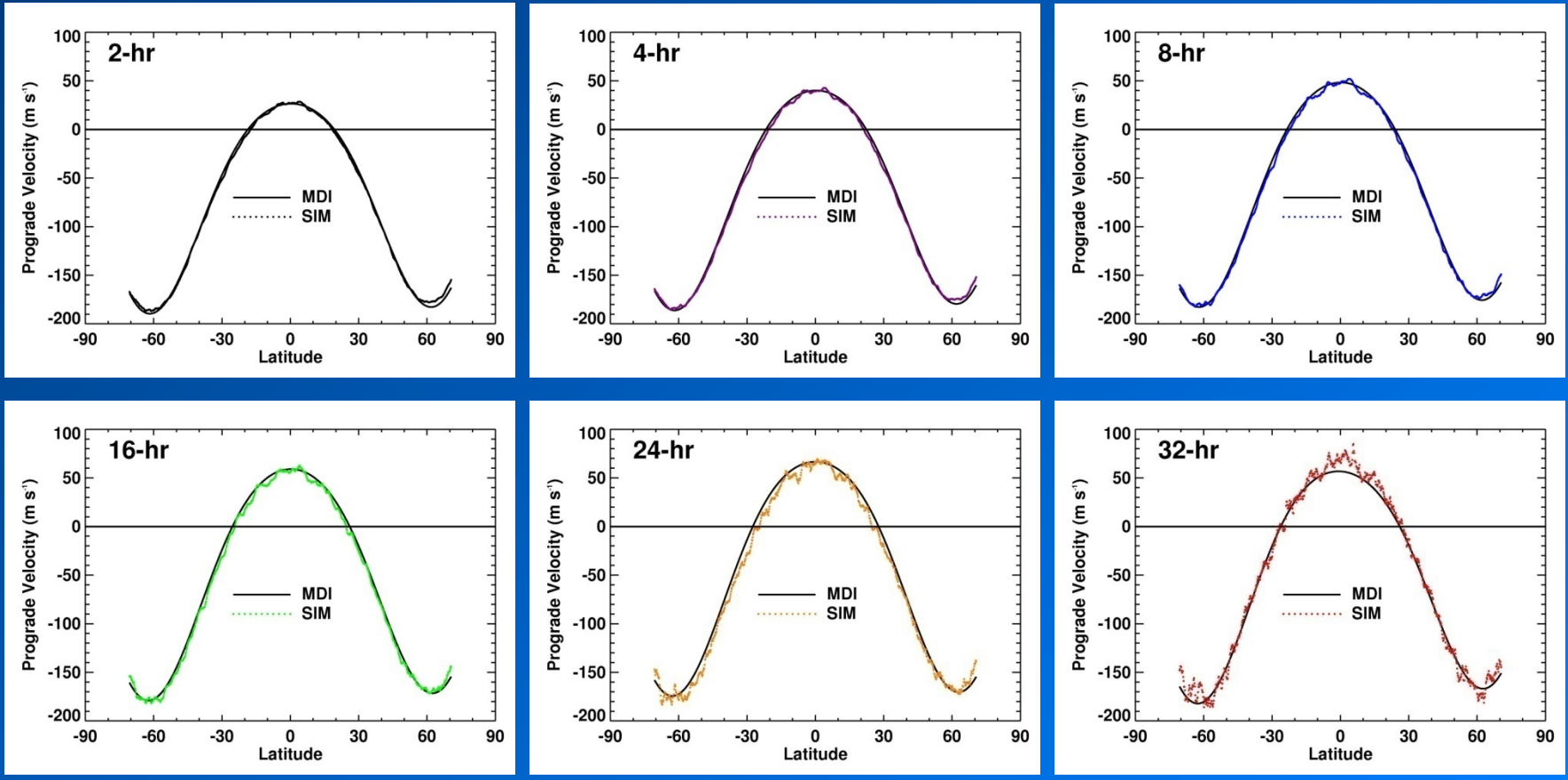

Reproducing their Meridional Flow

The latitudinal motions of the cellular patterns can be reproduced by making systematic changes to the complex spectral coefficient **amplitudes** (Hathaway et al. 2010). Black lines are polynomial fits to the observed signal. The colored dots in each diagram are measured from the simulation.

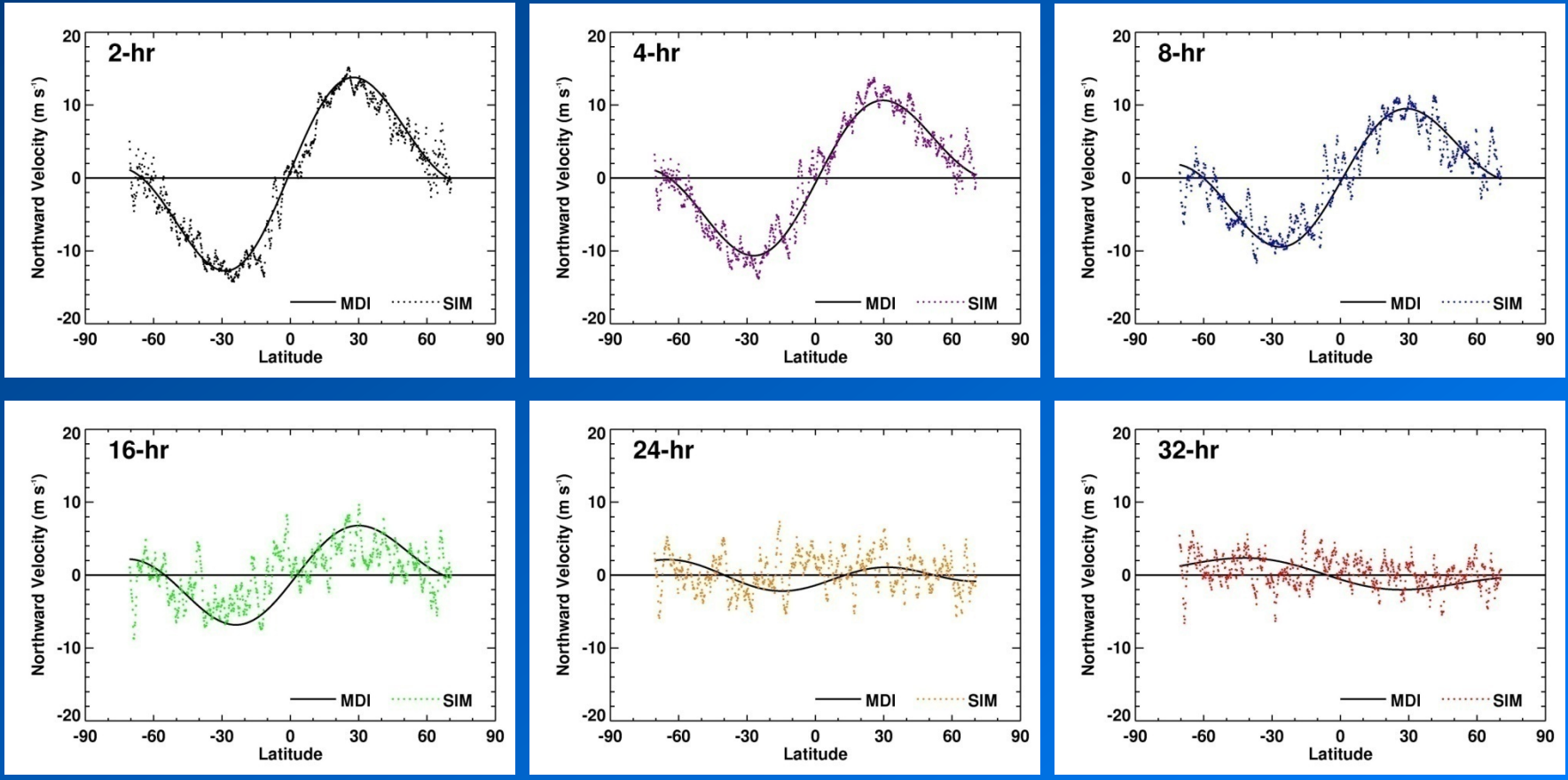

Reproducing the Lifetimes

The cellular structures are given finite lifetimes by adding random perturbations to the phases of the complex spectral coefficients. The amplitude of the perturbation was inversely proportional to a lifetime given by the size of the cell (from its wavenumber) divided by its flow velocity (from the amplitude of the spectral coefficient).

This process can largely reproduce the strength of the cross-correlation as a function of both time and latitude.

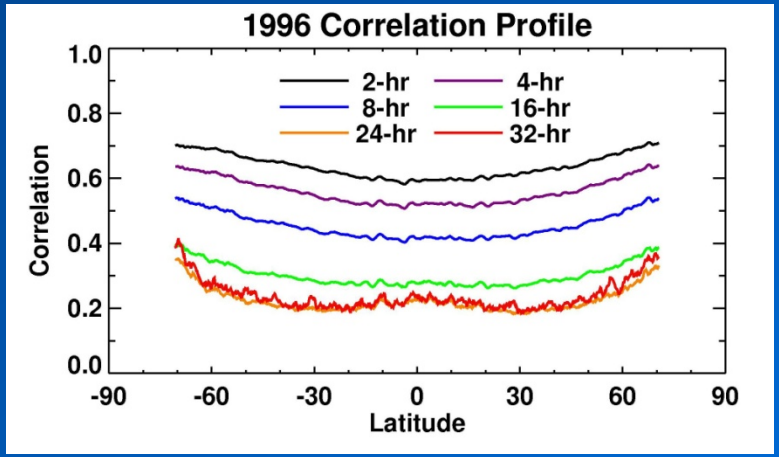

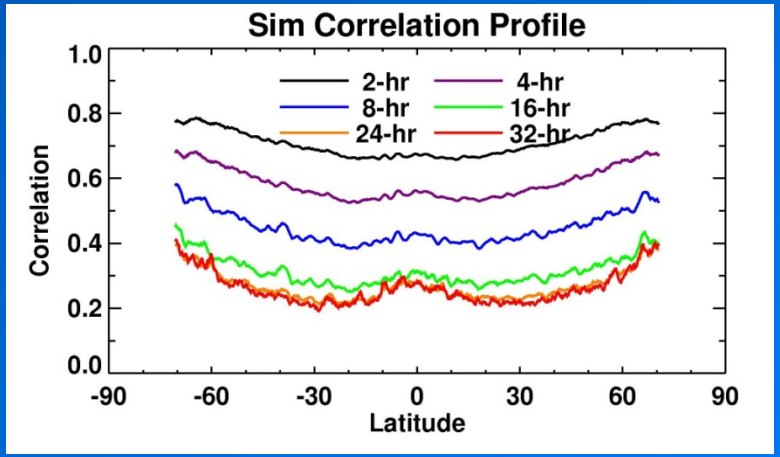

The Axisymmetric Flows

We (Hathaway & Rightmire 2010, *Science*, 327, 1350) measured the axisymmetric transport of magnetic flux by cross-correlating 11x600 pixel strips at 860 latitude positions between ±75° from magnetic images acquired at 96-minute intervals by MDI on SOHO.

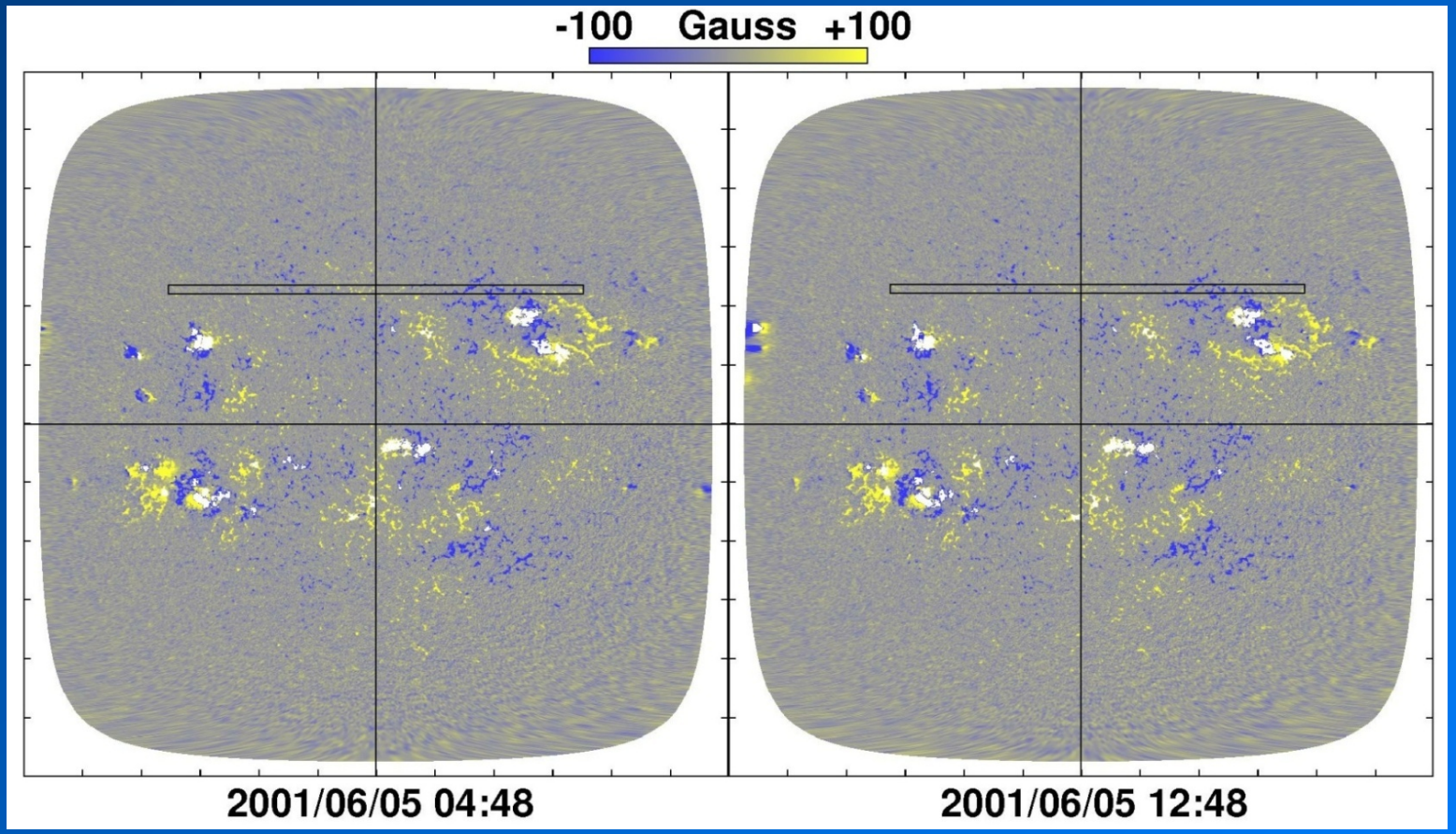

Average Flow Profiles

Our MDI data included corrections for CCD misalignment, image offset, and a 150 year old error in the inclination of the ecliptic to the Sun's equator. We extracted differential rotation and meridional flow profiles from over 60,000 image pairs from May of 1996 to September of 2010.

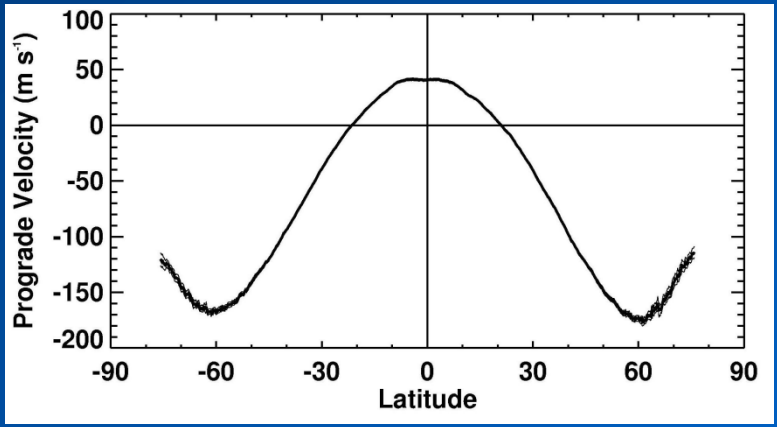

Average (1996-2010) differential rotation profile with 2σ error limits.

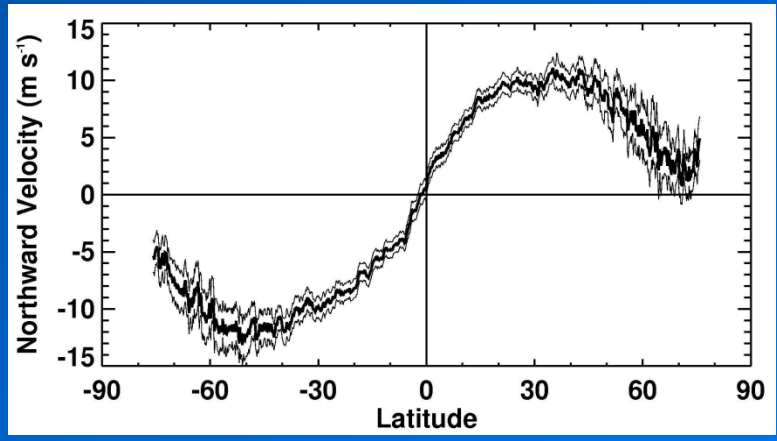

Average (1996-2010) meridional flow profile with 2σ error limits.

Axisymmetric Flow Profiles

Rightmire-Upton, Hathaway, & Kosak (2012) extended the measurements to HMI data and compared the results to the MDI measurements. The flow profiles are in good agreement but with small, significant, differences – DR is faster in HMI, MF is slower in HMI.

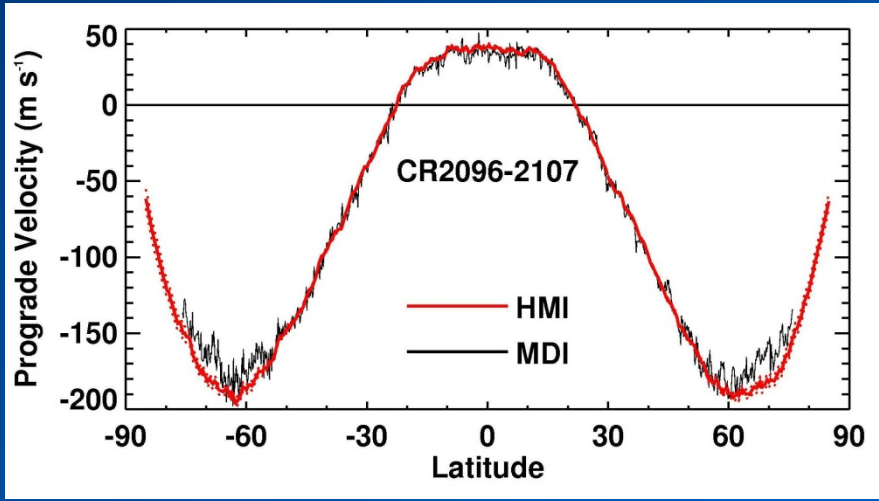

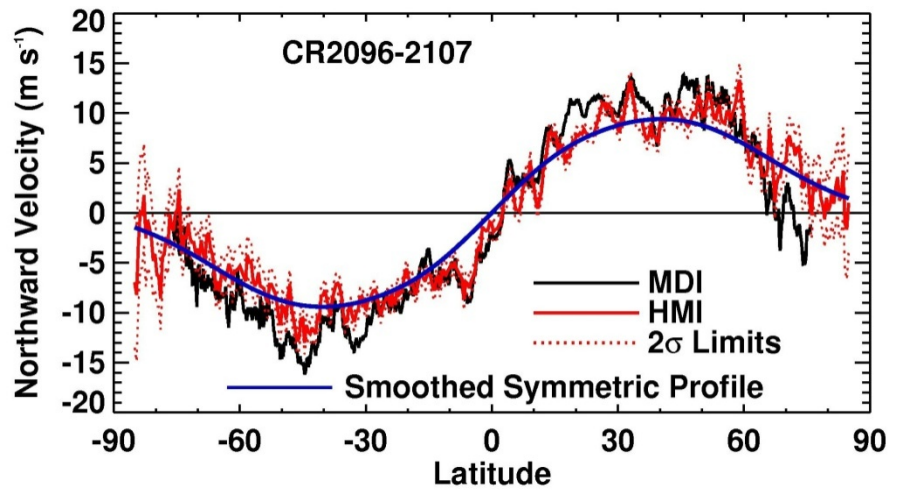

The average Differential Rotation profiles with 2σ error limits for the MDI/HMI overlap interval.

The average Meridional Flow profiles with 2σ error limits for the MDI/HMI overlap interval.

Meridional Flow Comparisons

The Meridional Flow we measure is very unlike that still used by the NRL group (Wang et al.). It is similar at low latitudes to that used by other groups but differs by not vanishing at high latitudes.

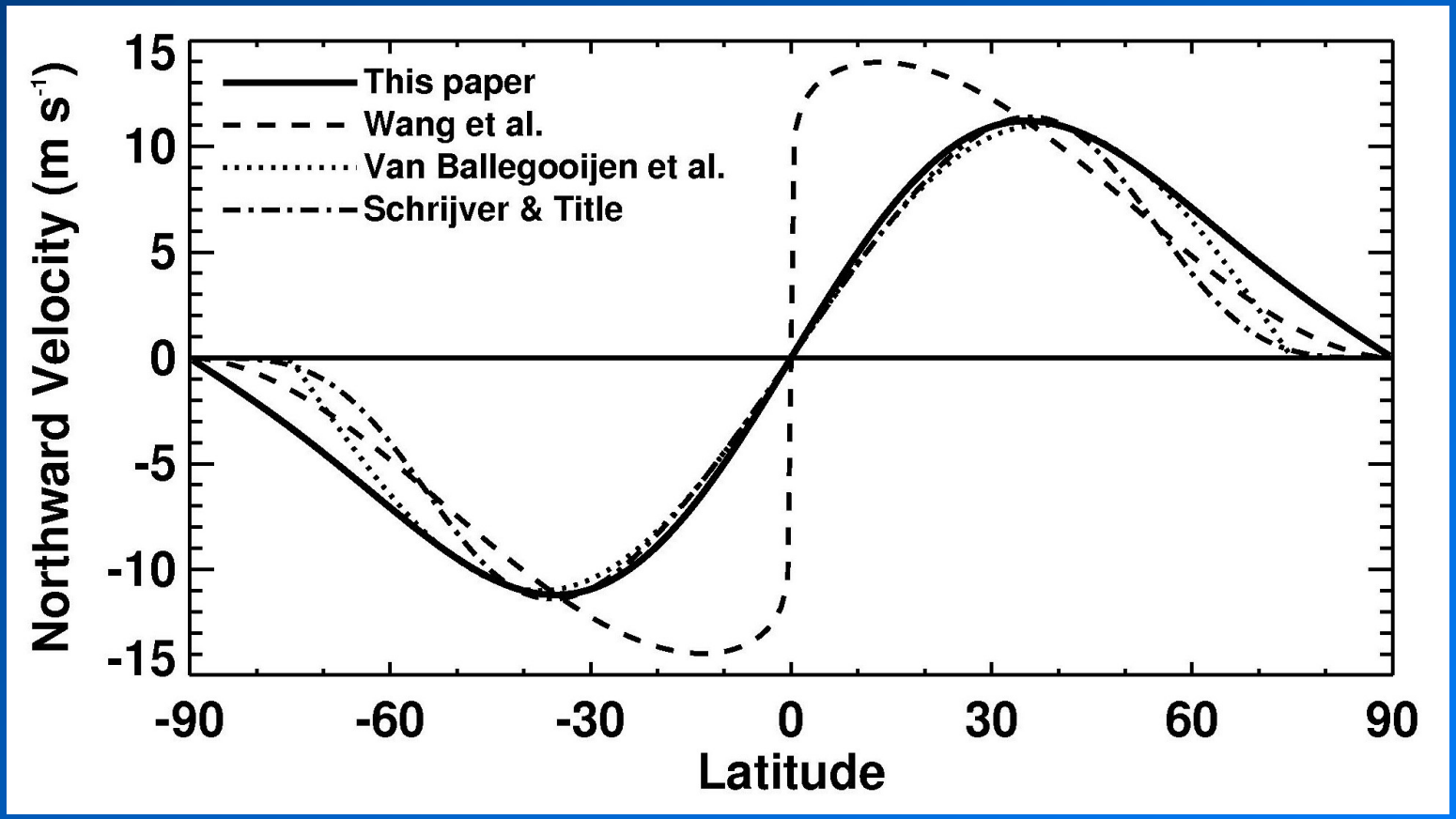

Solar Cycle Variations in the Axisymmetric Flows

While the differential rotation does vary slightly over the solar cycle, it is the meridional flow that shows the most significant variation. The Meridional Flow slowed from 1996 to 2001 but then increased in speed again after maximum. The slowing of the meridional flow at maximum seems to be a regular solar cycle occurrence (Komm, Howard, & Harvey, 1993). The greater speed up after maximum is specific to Cycle 23.

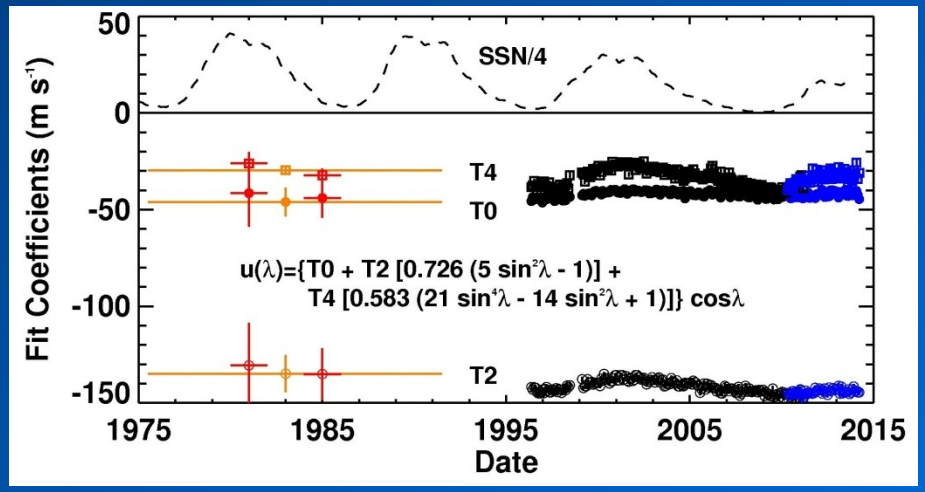

Differential rotation variations

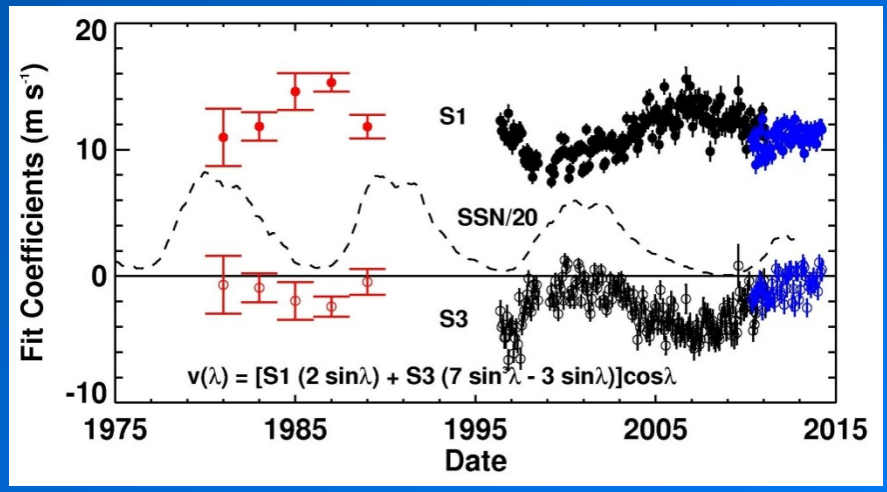

Meridional flow variations

Solar Cycle Variations in Flow Structure

The differential rotation and meridional flow profiles for each solar rotation also show that the differential rotation changes very little while the meridional flow changes substantially. The change in the meridional flow is primarily a weakening of the poleward flow poleward of the active latitudes that was strong in Cycle 23 and weak in Cycle 24.

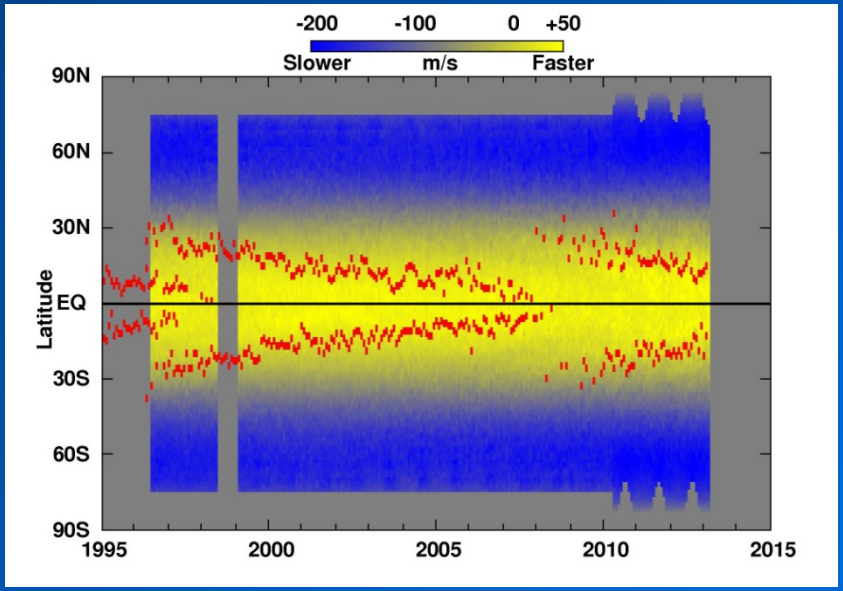

Differential rotation profiles

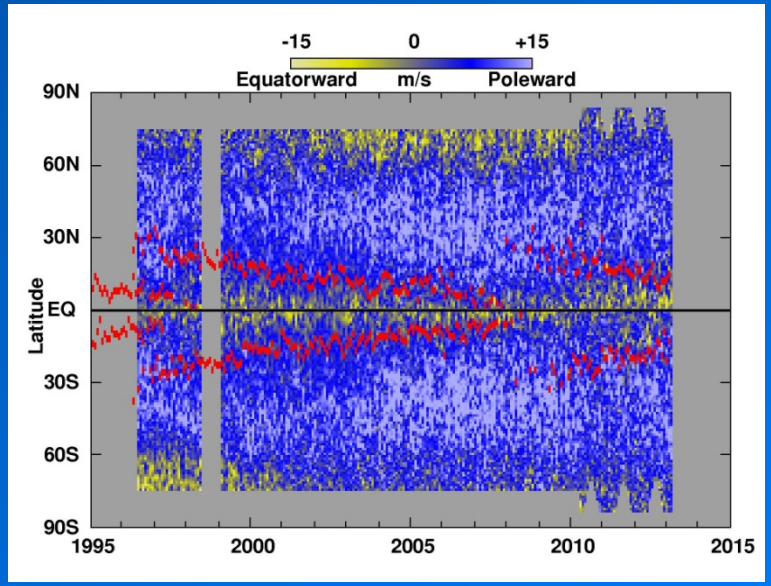

Meridional flow profiles

Modeling the Transport

The Flux Transport Equation

$$\frac{\partial B_r}{\partial t} = -\frac{1}{R_\odot \sin\theta}\frac{\partial}{\partial \phi}(uB_r) - \frac{1}{R_\odot \sin\theta}\frac{\partial}{\partial \theta}(vB_r \sin\theta)$$

$$+ \eta_H \left[\frac{1}{R_\odot^2 \sin\theta}\frac{\partial}{\partial \theta}\left(\sin\theta \frac{\partial B_r}{\partial \theta}\right) + \frac{1}{R_\odot^2 \sin^2\theta}\frac{\partial^2 B_r}{\partial \phi^2} \right]$$

$$+ S(\theta, \phi, t)$$

B_r is the radial component of the magnetic field.

Velocities (u, v) are functions of both ϕ and θ.

The diffusivity (η_H) is added to minimize Gibbs ringing.

The source term (S) is in the form of pairs of Gaussian flux concentrations representing active regions.

Earth-side Data Assimilation

Data from the visible hemisphere is assimilated with weights inversely proportional to the noise level (wt = cos ρ). Weights for previous synchronic map data decay with time with a latitude dependent decay time ($\tau = 27^d/[4 \cos B]$).

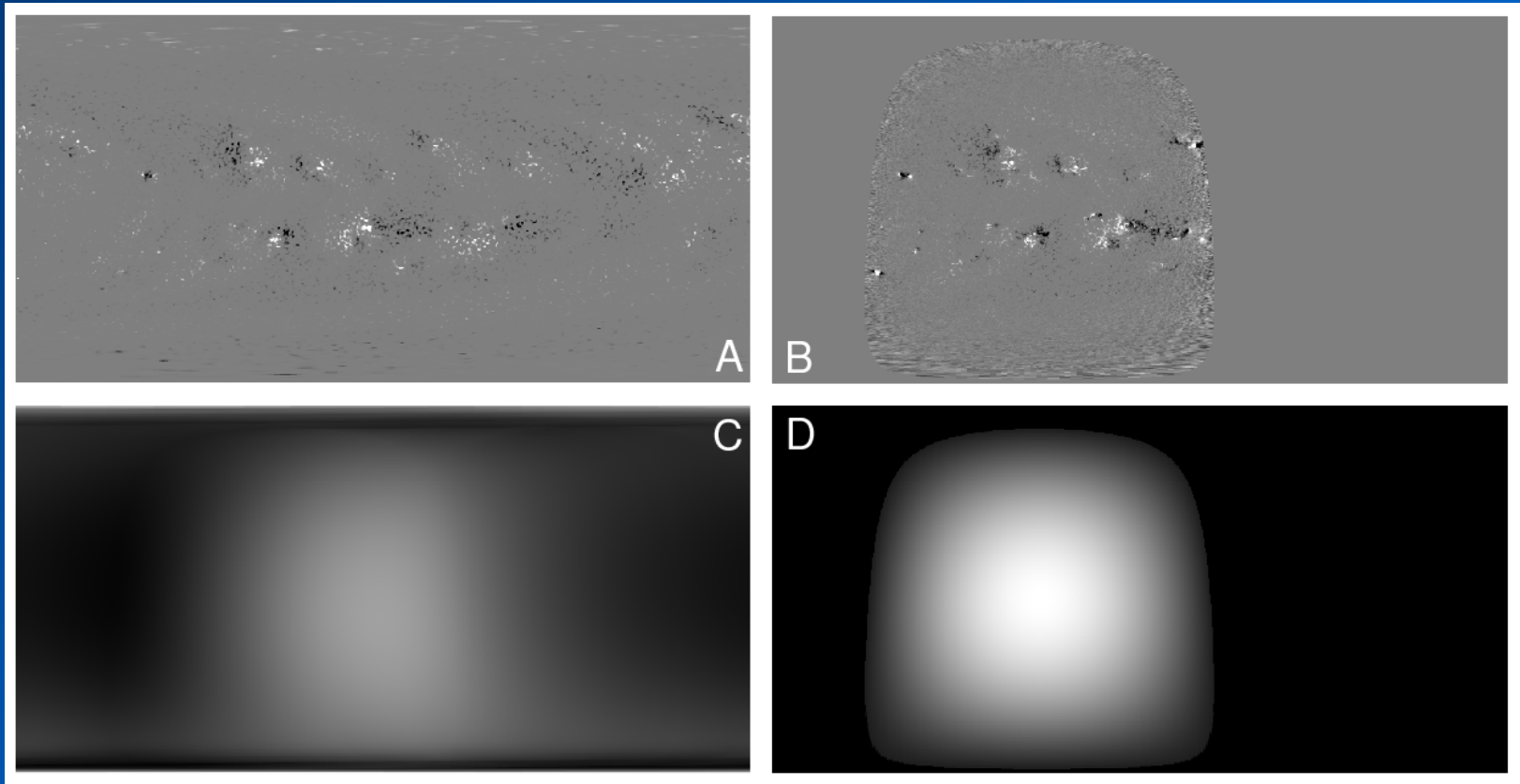

A) Previous synchronic map. B) Current magnetogram. C) The weights for the previous data. D) The weights for the current data.

Active Region Sources

We have data for daily sunspot group areas and positions extending back to 1874. We can use this to estimate active region sources of flux by using set relationships between group area and flux and the relative positions of the preceding and following sunspots.

Magnetic Flux

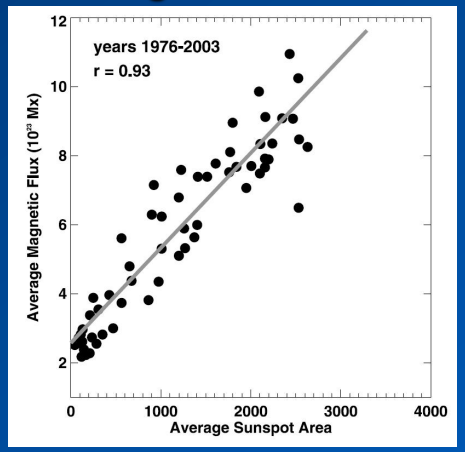

Dikpati, deToma, & Gilman (2006)

Longitudinal Separation

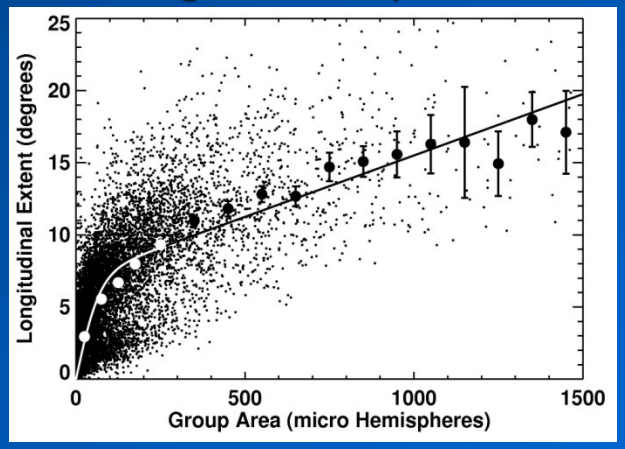

Upton & Hathaway (2013)

Latitudinal Separation

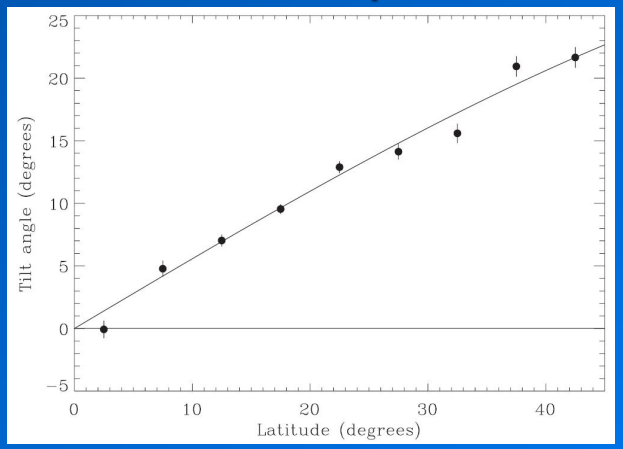

Stenflo & Kosovichev (2012)

We use the magnetic flux, the longitudinal separation , and the latitudinal separation appropriate for a sunspot group's area and latitude to place two Gaussian shaped flux sources for the preceding and following spots.

Finite Differencing

First order in time, second order in space.

Grid points are equi-spaced in latitude:

$\Delta\theta = \pi/512$

Longitudinal spacing changes with latitude:

$\Delta\phi = 2\pi/\{1024, 512, 128, 64, 32, 16, 8\}$

CFL condition set by convective flow velocities of ~500 m/s:

$\Delta t \sim 15$ minutes

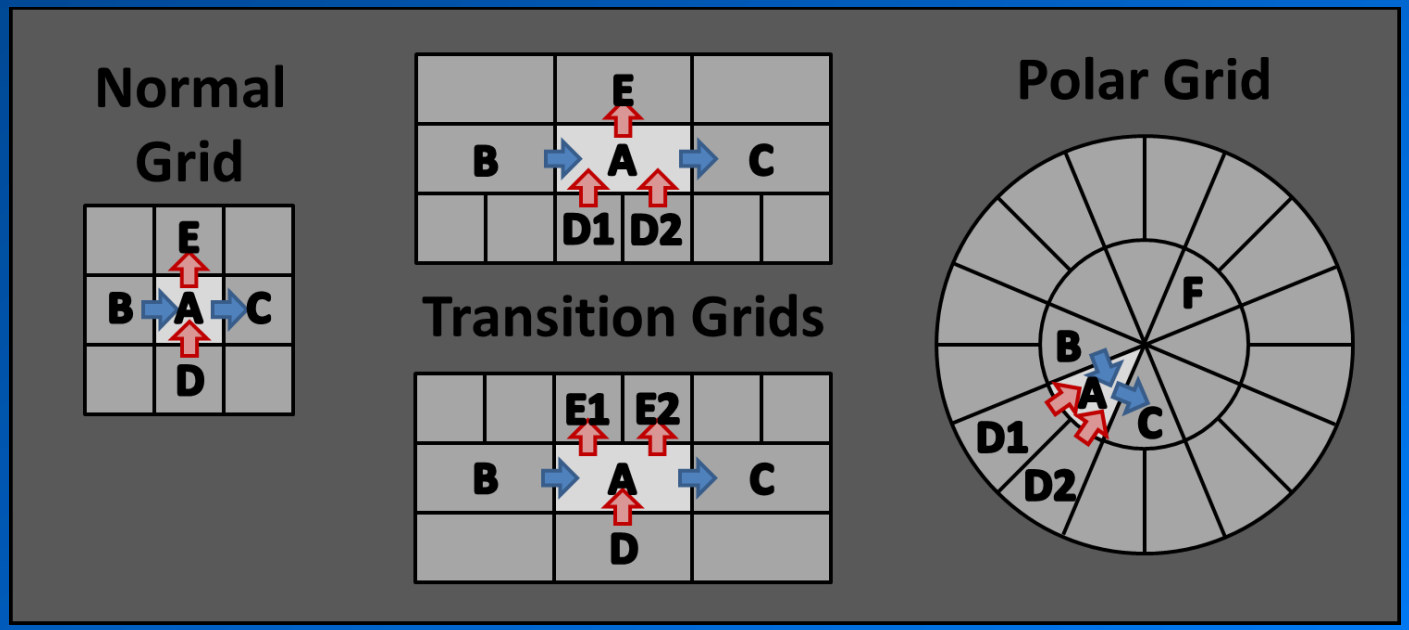

Surface Flux Transport

New magnetic field erupts through the surface in sunspot groups. The field is stripped from the sunspots by the convective motions and transported across the surface by the flows at and just below the surface – differential rotation, poleward meridional flow, and random shuffling by the supergranules. In the simulation shown below (for the year 2001) newly observed data is assimilated in the moving window.

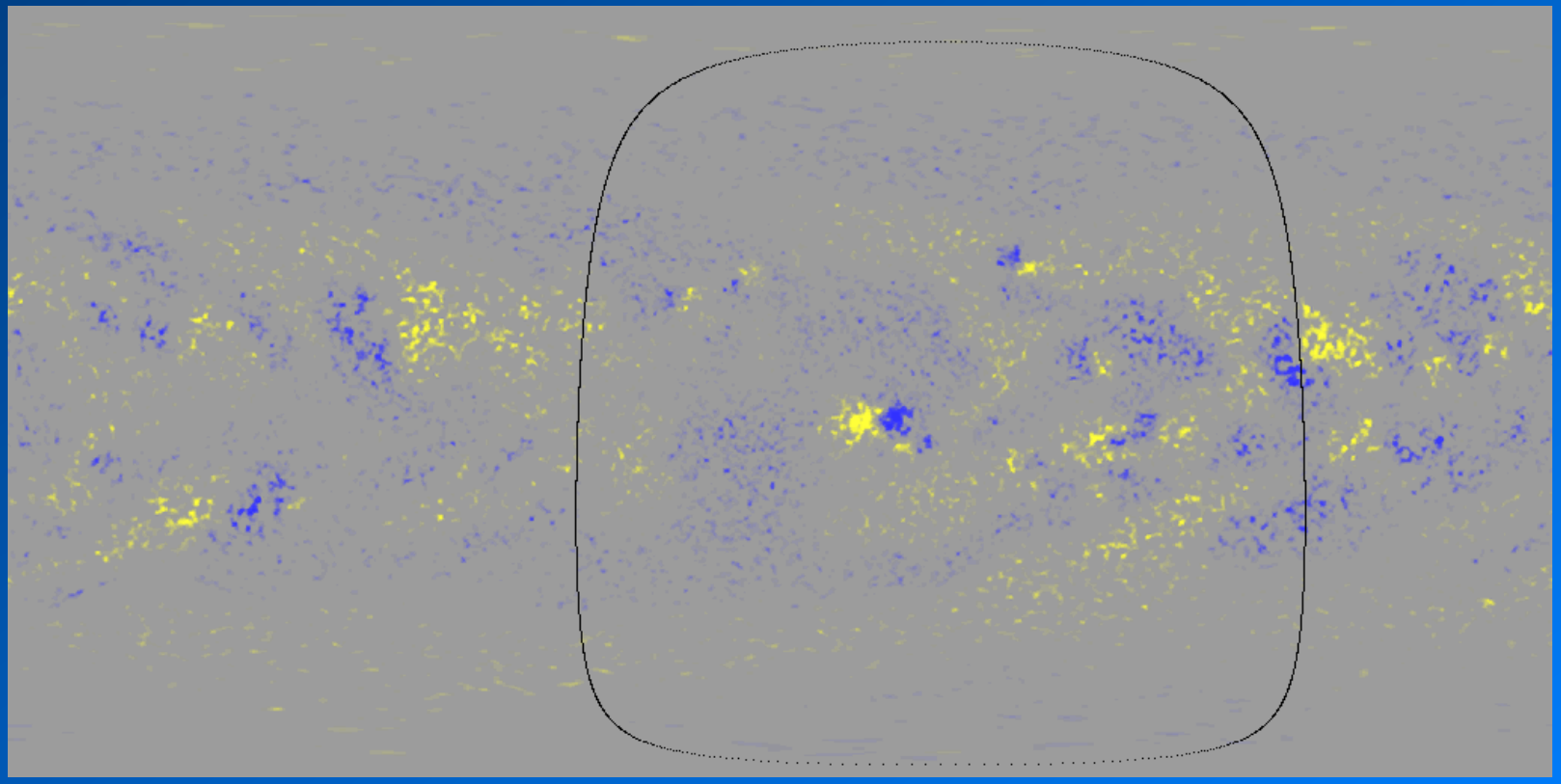

2001 South Pole Reversal

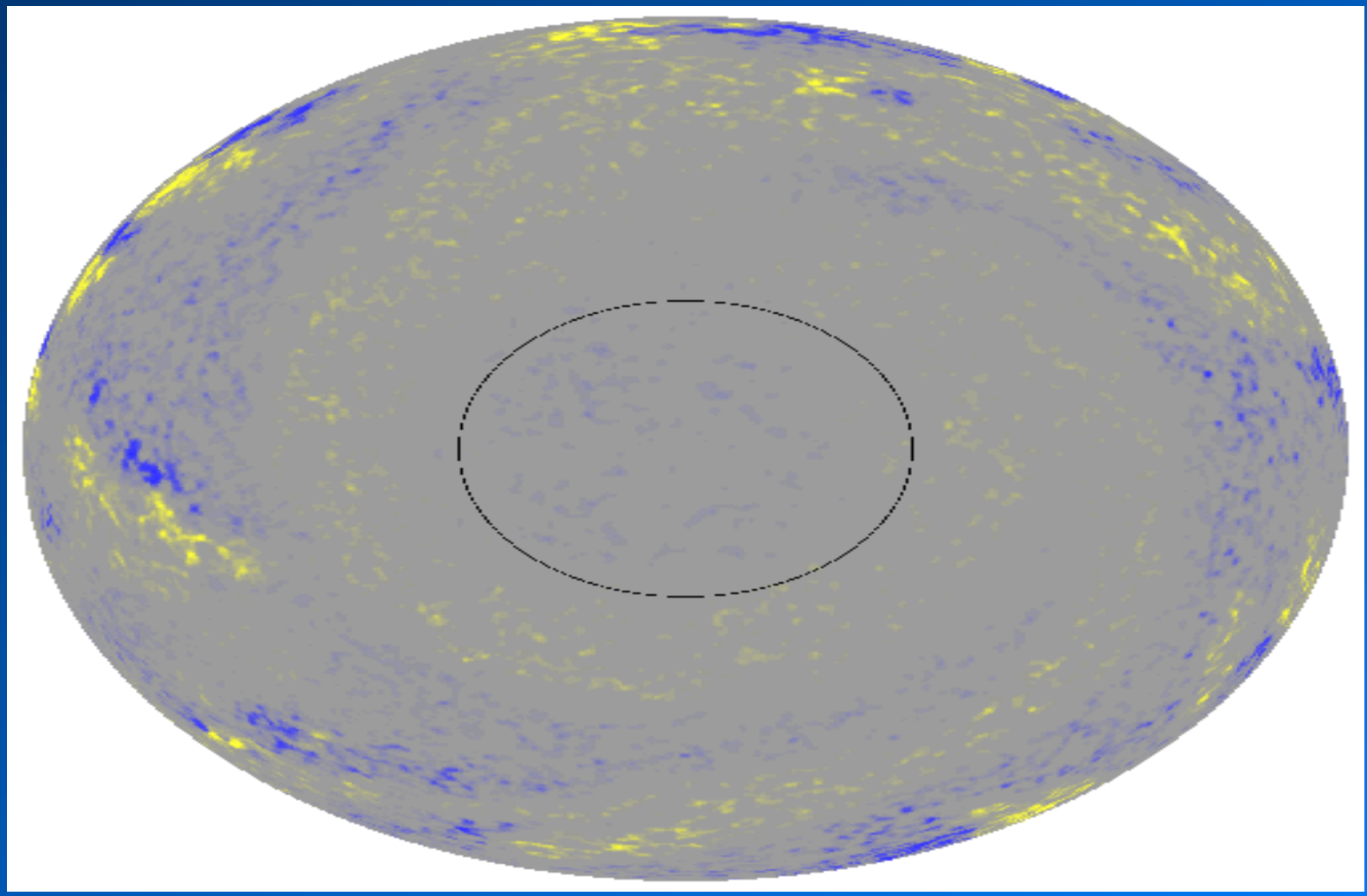

Simulations

Upton & Hathaway ApJ (2014) in press

- **Constant N-S symmetric Meridional Flow**
- **Observed Meridional Flow (varies in time & hemisphere)**
- **Amplified Meridional Flow Variations (varies in time & hemisphere)**

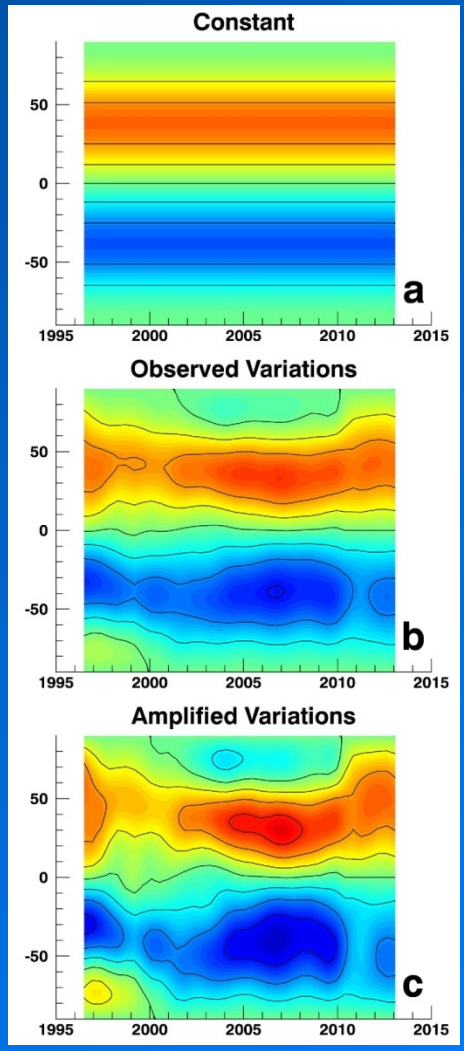

Red is northward flow and blue is southward flow. For reference the contours (black lines) show 0, ±5, ±10,±15 m s^{-1}.

Results

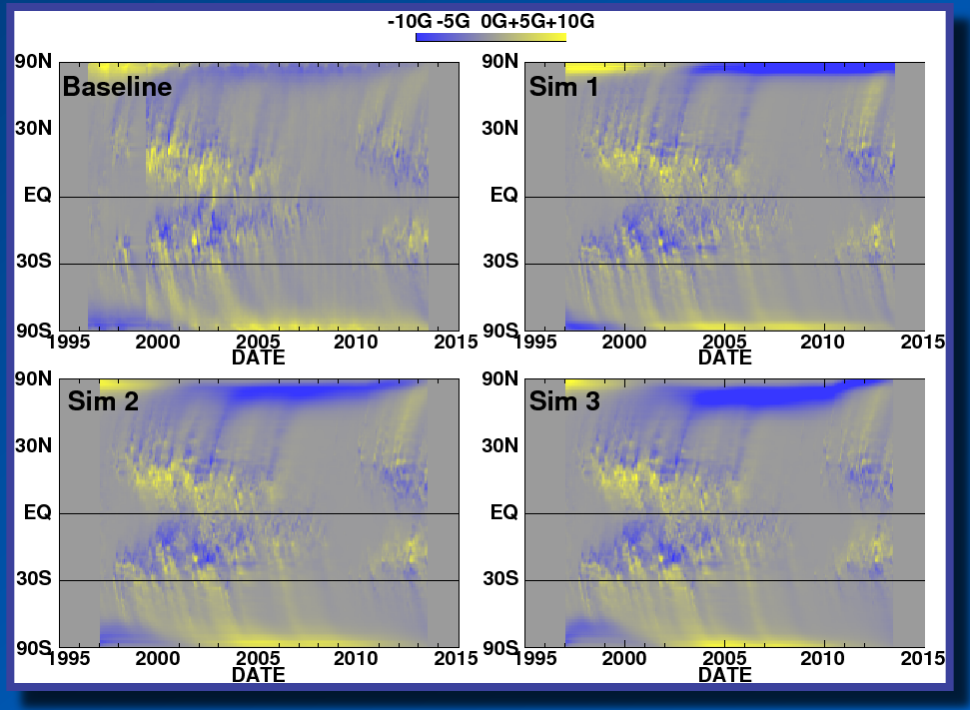

- The polar concentrations occur at lower latitudes for Sim 2 and Sim 3 when countercells are present in the meridional flow (in the south prior to 2000 and in the north from 2000 to 2010).
- The fact that this is not observed in the baseline, nor with the HMI data, suggests that these polar countercells are not real.

Results

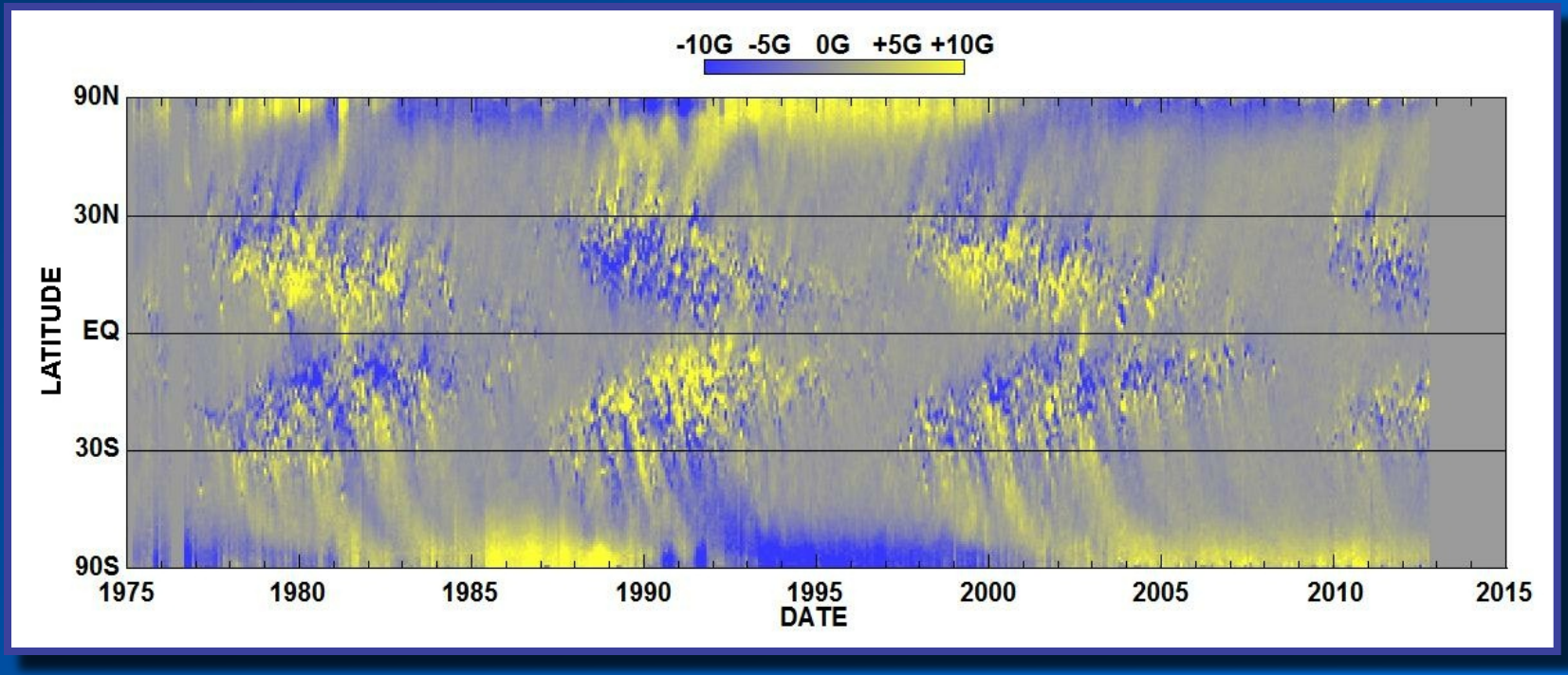

- Furthermore, polar concentrations offset from the poles have not been observed in the entire magnetic history of the Sun.
- This suggests that no polar countercells have been present in the last 40 years.

Results

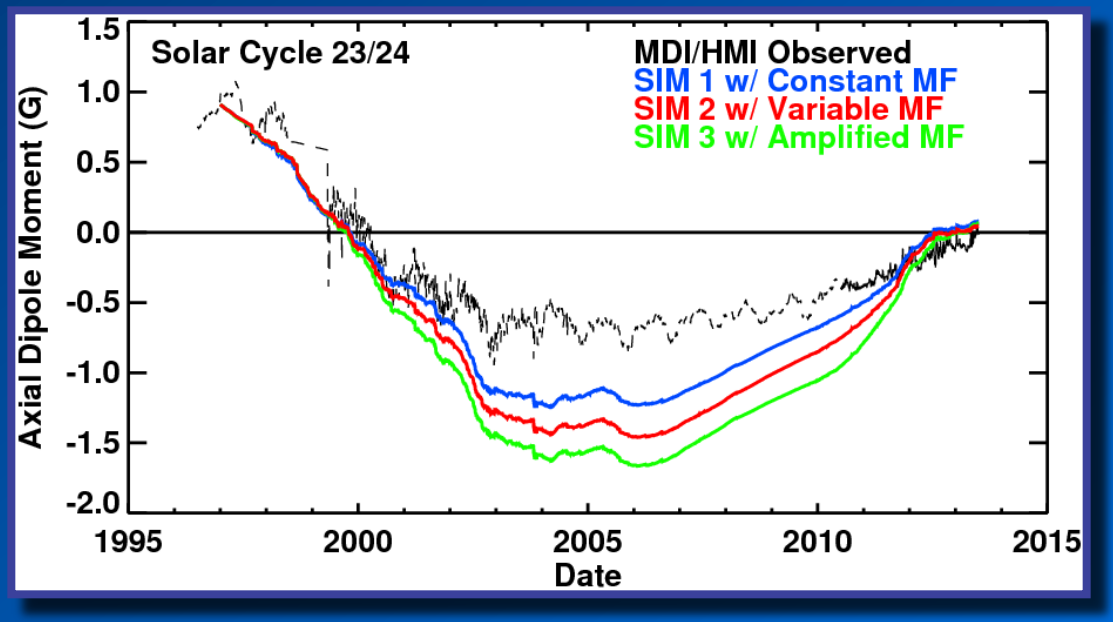

- The dipole moments in the simulations reach amplitudes about twice as strong as the observed axial dipole moment.
- Remarkably (and despite this) the timing of the Solar Cycle 24 reversal is accurate to within about a year.
- This suggests that the active region sources are being over-estimated for both the Solar Cycle 23/24 buildup and the Cycle 24 reversal.

Results

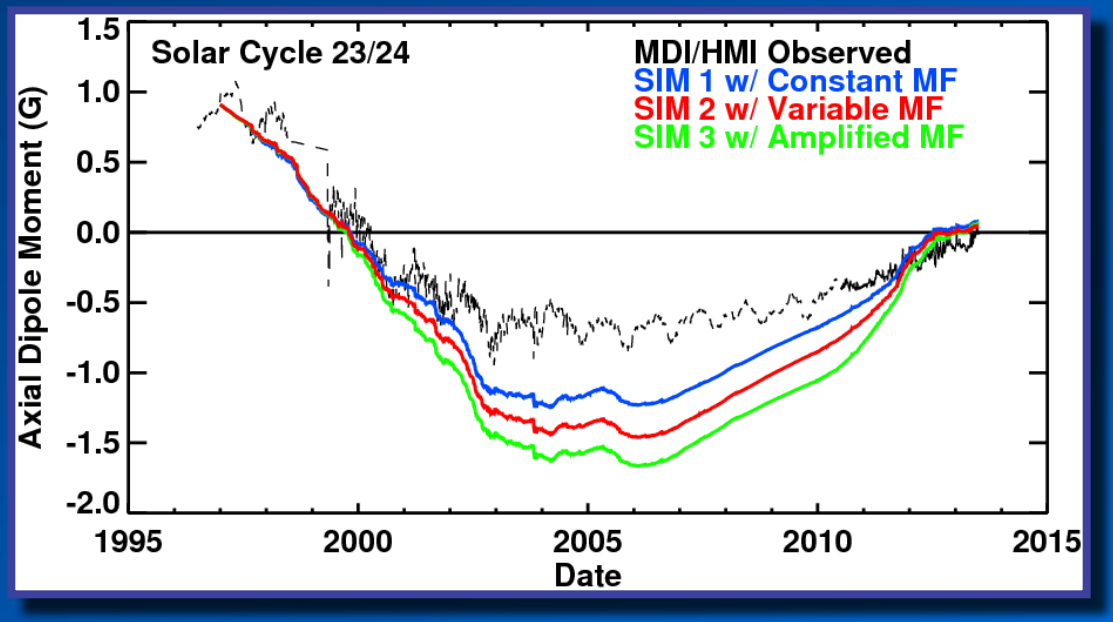

- The simulations show that the variations in the MF over Cycle 23 have a significant impact (at least ~20%) on the polar fields
- Surprisingly, rather than producing weaker polar fields, the variable meridional flow produced a stronger axial dipole moment.
- This suggests that the cause of the weak polar fields at the end of Cycle 23 should be attributed to the emergence of fewer active region sources.

Results

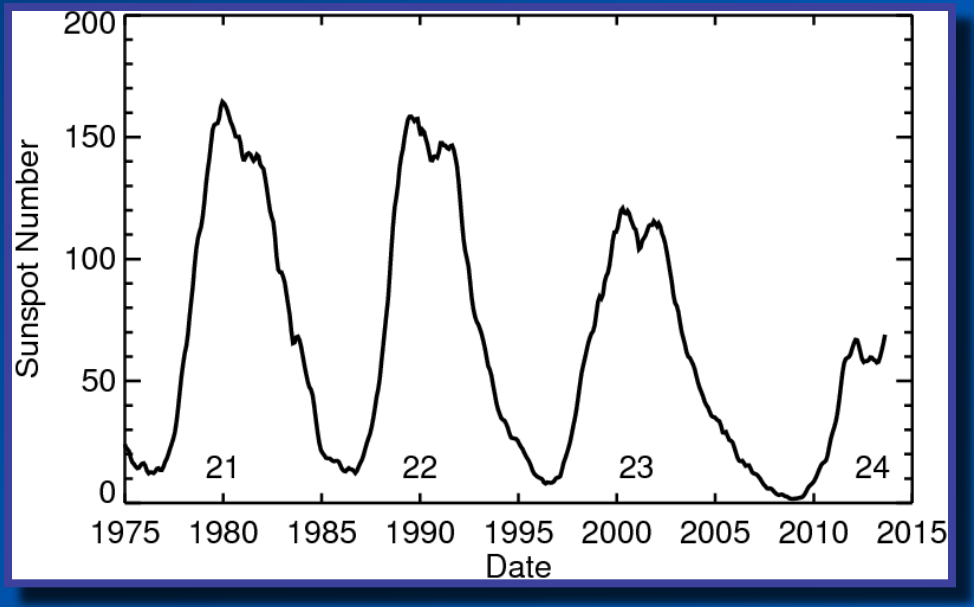

- Cycle 23 had a peak sunspot number of ~120 - much smaller that Cycle 21 and Cycle 22, which had peaks of ~160.
- With fewer sunspots to reverse the strong polar field of Cycle 22, there was insufficient flux remaining to rebuild a strong polar field.
- The subsequently weak polar fields of the Cycle 23/24 minimum then went on to produce the weak Cycle 24.

Newest Results

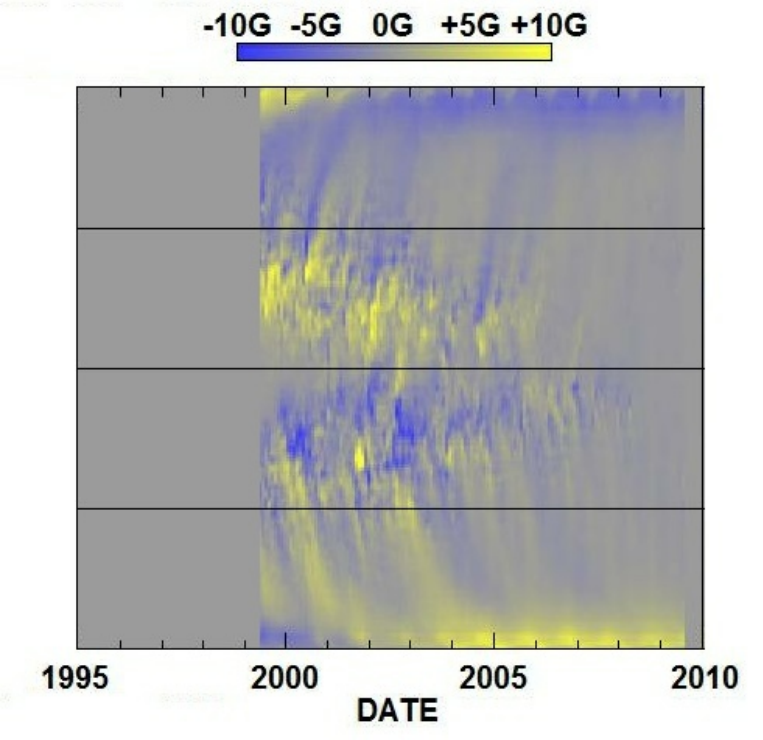

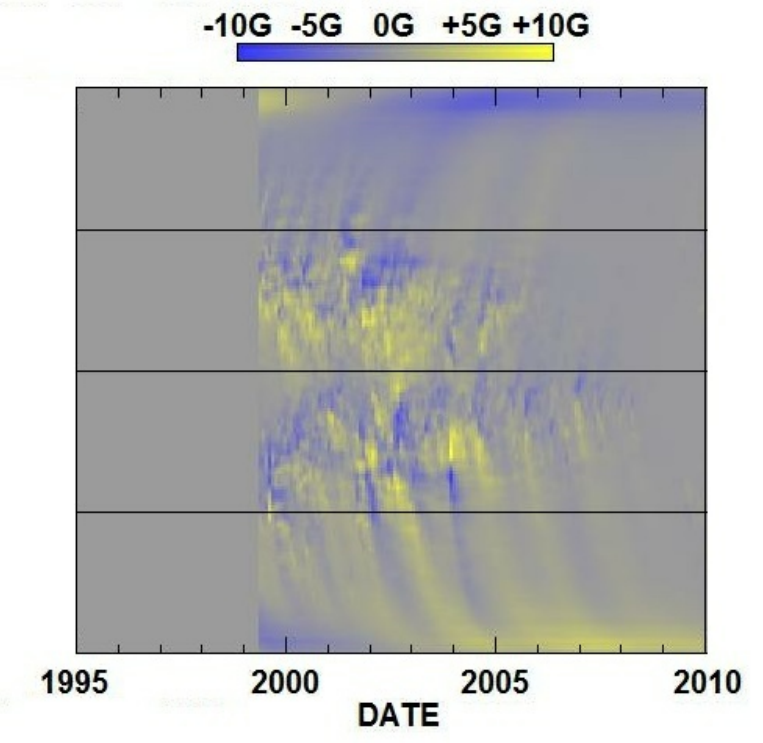

- We are constructing a database with MDI/HMI Active Region leading and following polarity magnetic flux centers of gravity.
- Flux transport with ONLY Active Region sources reproduces most of the details in the magnetic butterfly diagram.

Conclusions

- A “Fully Advective” flux transport model can be used to produce Synchronic Maps of the Sun’s magnetic field – of use as the inner boundary condition for space weather

- Flux transport using observed flows and active region sources still seems to be capable of explaining half of the solar dynamo problem – the production of the polar fields.